

Electronic ISSN: 1309-0267



**International Journal  
of Engineering &  
Applied Sciences**

**I  
J  
E  
A  
S**

**IJEAS**

**Volume 15, Issue 4  
2023**

Published by Akdeniz University

## **HONORARY EDITORS**

*(in alphabetical order)*

- Prof. Atluri, S.N.- University of California, Irvine-USA  
Prof. Liew, K.M.- City University of Hong Kong-HONG KONG  
Prof. Lim, C.W.- City University of Hong Kong-HONG KONG  
Prof. Liu, G.R.- National University of Singapore- SINGAPORE  
Prof. Nath, Y.- Indian Institute of Technology, INDIA  
Prof. Omurtag, M.H. -ITU  
Prof. Reddy, J.N.-Texas A& M University, USA  
Prof. Saka, M.P.- University of Bahrain-BAHRAIN  
Prof. Shen, H.S.- Shanghai Jiao Tong University, CHINA  
Prof. Xiang, Y.- University of Western Sydney-AUSTRALIA  
Prof. Wang, C.M.- National University of Singapore- SINGAPORE  
Prof. Wei, G.W.- Michigan State University-USA

## **EDITOR IN CHIEF:**

Assoc. Prof. Ibrahim AYDOGDU -Akdeniz University *aydogdu@akdeniz.edu.tr*

## **ASSOCIATE EDITORS:**

Assist. Prof. Kadir MERCAN –Mehmet Akif Ersoy  
University *kmercan@mehmetakif.edu.tr*

## **SECTION EDITORS:**

- Assoc. Prof. Metin Mutlu Aydın – Ondokuz Mayıs University  
Assoc. Prof. Mustafa Arda –Trakya University  
Assist. Prof. Refik Burak Taymuş- Van 100. Yıl University

## EDITORIAL BOARD

*(The name listed below is not Alphabetical or any title scale)*

Prof. Xinwei Wang -Nanjing University of Aeronautics and Astronautics

Asst. Prof. Francesco Tornabene -University of Bologna

Asst. Prof. Nicholas Fantuzzi -University of Bologna

Assoc. Prof. Keivan Kiani - K.N. Toosi University of Technology

Asst. Prof. Michele Baccocchi -University of Bologna

Asst. Prof. Hamid M. Sedighi -Shahid Chamran University of Ahvaz

Prof. Yaghoub Tadi Beni -Shahrekord University

Prof. Raffaele Barretta -University of Naples Federico II

Prof. Meltem ASİLTÜRK -Akdeniz University *meltemasilturk@akdeniz.edu.tr*

Prof. Metin AYDOĞDU -Trakya University *metina@trakya.edu.tr*

Prof. Ayşe DALOĞLU - KTU *aysed@ktu.edu.tr*

Prof. Oğuzhan HASANÇEBİ - METU *oguzhan@metu.edu.tr*

Asst. Prof. Rana MUKHERJİ - The ICFAI University

Assoc. Prof. Baki ÖZTÜRK - Hacettepe University

Assoc. Prof. Yılmaz AKSU -Akdeniz University

Assoc. Prof. Hakan ERSOY- Akdeniz University

Assoc. Prof. Mustafa Özgür YAYLI -Uludağ University

Assoc. Prof. Selim L. SANİN - Hacettepe University

Asst. Prof. Engin EMSEN -Akdeniz University

Prof. Serkan DAĞ - METU

Prof. Ekrem TÜFEKÇİ - İTÜ

## ABSTRACTING & INDEXING



IJEAS provides unique DOI link to every paper published.

### EDITORIAL SCOPE

The journal presents its readers with broad coverage across some branches of engineering and science of the latest development and application of new solution algorithms, artificial intelligent techniques innovative numerical methods and/or solution techniques directed at the utilization of computational methods in solid and nano-scaled mechanics.

International Journal of Engineering & Applied Sciences (IJEAS) is an Open Access Journal

International Journal of Engineering & Applied Sciences (IJEAS) publish original contributions on the following topics:

**Civil Engineering:** numerical modelling of structures, seismic evaluation, experimental testing, construction and management, geotechnical engineering, water resources management, groundwater modelling, coastal zone modelling, offshore structures, water processes, desalination, waste-water treatment, pavement and maintenance, transport and traffic, laser scanning, and hydrographic surveying, numerical methods in solid mechanics, nanomechanic and applications, microelectromechanical systems (MEMS), vibration problems in engineering, higher order elasticity (strain gradient, couple stress, surface elasticity, nonlocal elasticity)

**Electrical Engineering:** artificial and machine intelligence and robotics, automatic control, bioinformatics and biomedical engineering, communications, computer engineering and networks, systems security and data encryption, electric power engineering and drives, embedded systems, Internet of Things (IoT), microwaves and optics.

**Engineering Mathematics and Physics:** computational and stochastic methods, optimization, nonlinear dynamics, modelling and simulation, computer science, solid state physics and electronics, computational electromagnetics, biophysics, atomic and molecular physics, thermodynamics, geophysical fluid dynamics, wave mechanics, and solid mechanics.

**Mechanical Engineering:** machine design, materials science, mechanics of materials, manufacturing engineering and technology, dynamics, robotics, control, industrial engineering, ergonomics, energy, combustion, heat transfer, fluids mechanics, thermodynamics, turbo machinery, aerospace research, aerodynamics, and propulsion.

IJEAS allows readers to read, download, copy, distribute, print, search, or link to the full texts of articles.



# CONTENTS

<b>Investigation of Effect of W-Zn-Co Alloy on Microstructure And Hardness of The Epoxy Composites</b> <i>By Mikail Aslan</i> .....	144-149
<b>Dendrobranchiata Chitin Deacetylation Degree and its Potency as Iron (III) Ion Adsorbent from Aqueous Solution</b> <i>By Oluwashina Philips GBENEBOR, Abimbola Patricia Idowu POPOOLA</i> .....	150-162
<b>Large Deformation Analysis of Hyperelastic Continuum with Hexahedral Adaptive Finite Elements</b> <i>By Mustafa TEKİN, Bahadır ALYAVUZ</i> .....	163-183
<b>A Charging Station Planning Study to Prepare for the Utilization of Electric Vehicles on University Campuses: The Case of Ondokuz Mayıs University</b> <i>By Metin Mutlu AYDIN</i> .....	184-204



## Investigation of Effect of W-Zn-Co Alloy on Microstructure And Hardness of The Epoxy Composites

Mikail Aslan

Gaziantep University, Faculty of Engineering, Department of Metallurgical and Material Science Engineering, Gaziantep, 27310, Turkey

✉: [mikailsln@gmail.com](mailto:mikailsln@gmail.com), : 0000-0003-2235-5104-0000

Received:12.07.2023, Revised: 28.09.2023, Accepted: 28.10.2023

### Abstract

*This research investigates the production of epoxy resin composites reinforced by the synthesized heavy tungsten alloys (W-7Zn-3Co-Y<sub>2</sub>O<sub>3</sub>). Y<sub>2</sub>O<sub>3</sub> is used for dispersion of the compound during the ball milling process. Laminating resin component A and hardened component B were used to produce polymer epoxy matrix. The tungsten heavy alloys reinforced epoxy composites were examined in terms of Vickers hardness, density measurement and microstructural characterization. The results indicate that the 16 hour-milled reinforced epoxy composites have the highest hardness value.*

**Keywords:** Tungsten alloys, mechanical alloying, and polymer epoxy composites

### 1. Introduction

With extensive applications of polymer and its composites, epoxy resin polymer composites are extensively preferred in national economic construction and national defense construction works [1-3] due to their high specific strength-weight ratio, chemical, wear and corrosion resistance. Foreexample; epoxy resins can be employed as insulating systems in high-voltage applications, including cables, generators, motors, and cast resin dry-type transformers, among others [4]. Fiori et al. [5] conducted an assessment of how the inclusion of uniaxial basalt fabric layers impacts the mechanical properties of a glass mat/epoxy composite specifically designed for marine applications. Baig et al. focused on the hybrid epoxy composite coatings for tribological applications [6]. Also, epoxy composites can be alternative for aluminium, steel and titanium [7-9]. On the other hand, the application of pure epoxy resin is limited by its brittleness, small elongation and poor mechanical impact resistance [10, 11].

Many researchers found that the addition of nanoparticles into adhesives like epoxies improved the adhesive characteristics [12-14]. Conradi et al. [15] studied the dispersed silica nanoparticles into the epoxy matrix to produce a coating with a better hardness of 50% when compared with coatings of pure epoxy. Karippal et al. [16] used multi-walled carbon nanotubes (MWCNT) and carbon black (CB) as reinforcements with different fractions into the epoxy matrix and determine the change in hardness of the composite. Radwan et al. [17] studied the effect of reinforced epoxy risen by aluminum particles with variation in weight percentage and evaluated the change in vickers hardness, density, and the compression stress of the composites. Al fillers with higher percentages tend to increase the hardness of resulting composites when compared with pure epoxy resin. The study conducted by Halder et al. [18] demonstrated significant improvements in various mechanical properties of the epoxy system. The maximum enhancements observed were approximately 24% in tensile strength, 47% in tensile modulus, 48% in compressive strength,



44% in flexural strength, and an impressive 77% in flexural modulus compared to the neat epoxy system. In another study[19], researchers aimed to enhance the coating properties of epoxy resin by incorporating Ni–La–Fe–O nanoparticles in the form of  $\text{NiLa}_x\text{Fe}_{2-x}\text{O}_4$ /epoxy nanocomposites. To achieve this, they synthesized new composites with varying x compositions (x = 0.00, 0.50, 1.00, 1.50, and 2.00) in situ, while the epoxy resin was prepared using a straightforward solution method with ultrasonic assistance. The inclusion of Ni–Fe formulations demonstrated considerable potential in improving epoxy coatings.

In this paper, W-Zn7-3Co + %0.5  $\text{Y}_2\text{O}_3$  reinforcement particles were synthesized with different milling times and techniques before adding them into the epoxy resin matrix. Different samples were produced to investigate the effect of milling time on the hardness and density of epoxy matrix composites.

## 2. Materials and Methods

To produce W-Zr-Co- $\text{Y}_2\text{O}_3$  reinforced epoxy polymer composites, W, Zr, Co, and  $\text{Y}_2\text{O}_3$  particles and laminating resin component A and component B were supplied from Nanografi, EGE nano A.Ş and ADS Chemistry, respectively. The heavy tungsten alloys were synthesized by mechanical alloy routine. There are two kinds of strategy were used to produce the heavy tungsten alloys, which are called the classic and alternative methods respectively. In the classical method, all raw materials are milled for 24 hours. In the second technique, initially, the Zn-Co compounds were milled for 24 hours. The W and  $\text{Y}_2\text{O}_3$  and the milled Zn-Co compounds were then milled for 8, 16, and 24 hours. The detailed information is given in previous study [20]. In the second technique, sample 1,2,3 and 4 are called according to their milling times of 0,8, 16 and 24 hours, respectively while the sample 5 is produced by classical method. To form heavy tungsten reinforced epoxy composites, the heavy tungsten alloy (0.5 g) and the epoxy (10 g) were weighted. The powder compounds and resin were placed in a beaker and the mixing was carried out by utilizing a mechanical stirrer for half-hour. The hardener is then poured into the beaker as the weight ratio between the resin and hardener of 2. The resulting suspension was mixed for 2 hours by a magnetic stirrer with a speed of 800 rpm. To ensure homogenous distribution, the compound was again mechanically mixed for 5 minutes and the compound was dried at room temperature.

## 3. Results and Discussion

Figure 1 shows the Vickers hardness of the pure epoxy and the heavy tungsten reinforced epoxy polymer composites with the force load of 0.3 kgf and the dwell time of 20 sec. Five measurements were applied for each sample to calculate the average value of the measurements. The addition of the tungsten metal powder as reinforcement material to the epoxy matrix leads to a noticeable increase in the microhardness value. Furthermore, the ball milling time of tungsten powder has a significant effect on the microhardness. The composite having 16-hour milled tungsten heavy alloy shows the best hardness value of 22.6 HV.

On the other hand, the effect of the second milling method was determined by comparing the two samples fabricated by using these two different strategies. The composites produced by the second one have approximately 25 % higher microhardness values when compared with the first one.

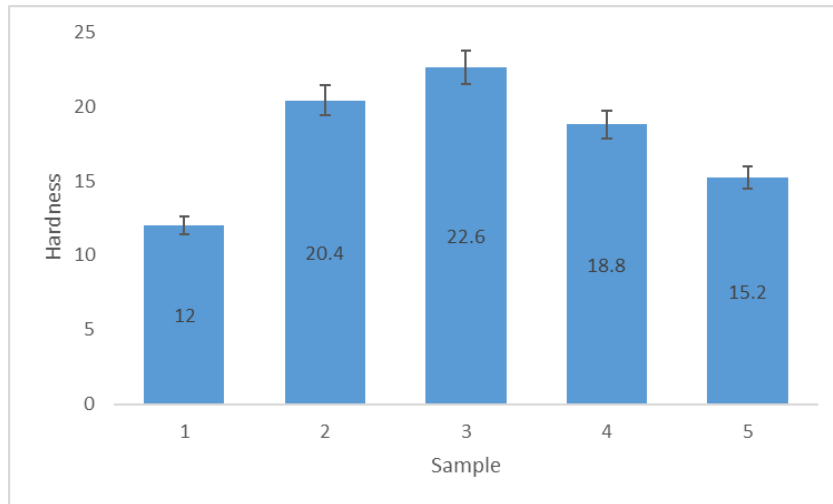


Fig. 1. The Vickers hardness values of the given epoxy composites

The density measurements are based on Archimedes' principle. The measured density of pure epoxy and the reinforced epoxy composites are shown in Figure 2. As expected, due to the nature of the high density of tungsten alloy, the addition of the synthesized tungsten alloy to the epoxy matrix increases the density of the composites since the density of the pure epoxy is the smallest value among them with a value of  $1.146 \text{ g/cm}^3$ . When regarding the polymer composites produced by the second method, the composite with the 8 hours milled alloy indicates the highest measured density value having value of  $1.198 \text{ g/cm}^3$ . This can be because pure tungstens powders are higher density values than the synthesized alloys, which means the 8-hour milled alloy may include the highest pure tungsten ratio when comparing the other milled alloys. On the other hand, In the classical method, as expected, the measured density is a slightly higher value than pure, and 16 and 24 hour milled alloyed reinforced epoxy composites.

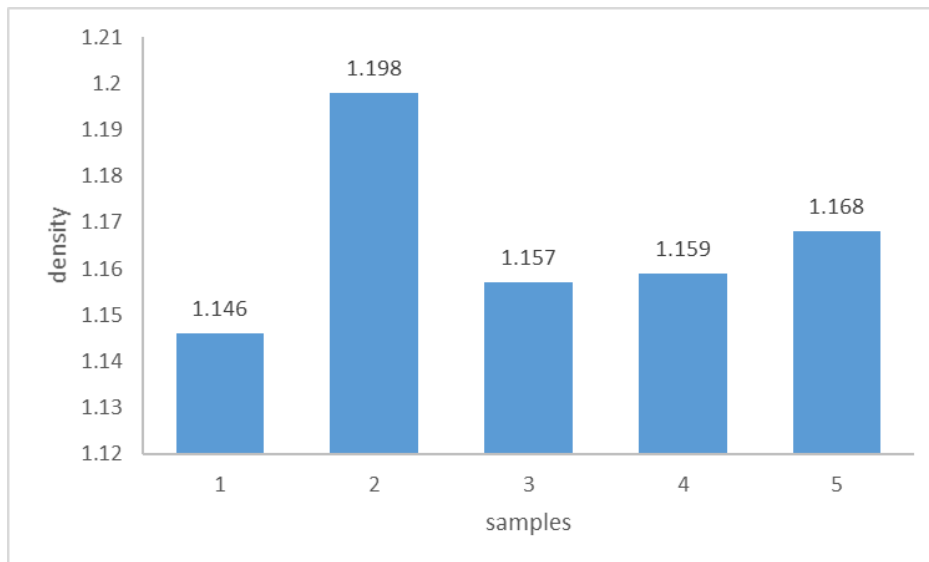


Fig. 2. The measured density of the given epoxy composites

Figure 3 illustrates optical microscope images of reinforced epoxy composites with varying milling times, showcasing different types of agglomerations across all structures. This is due to the differences between dimensions, interactions, and volume fractions of the neat epoxy and tungsten alloy. In contrast to the Vicker's results, the distribution of tungsten alloys in the 24-hour milled structures is superior to that of the 16-hour milled structures.



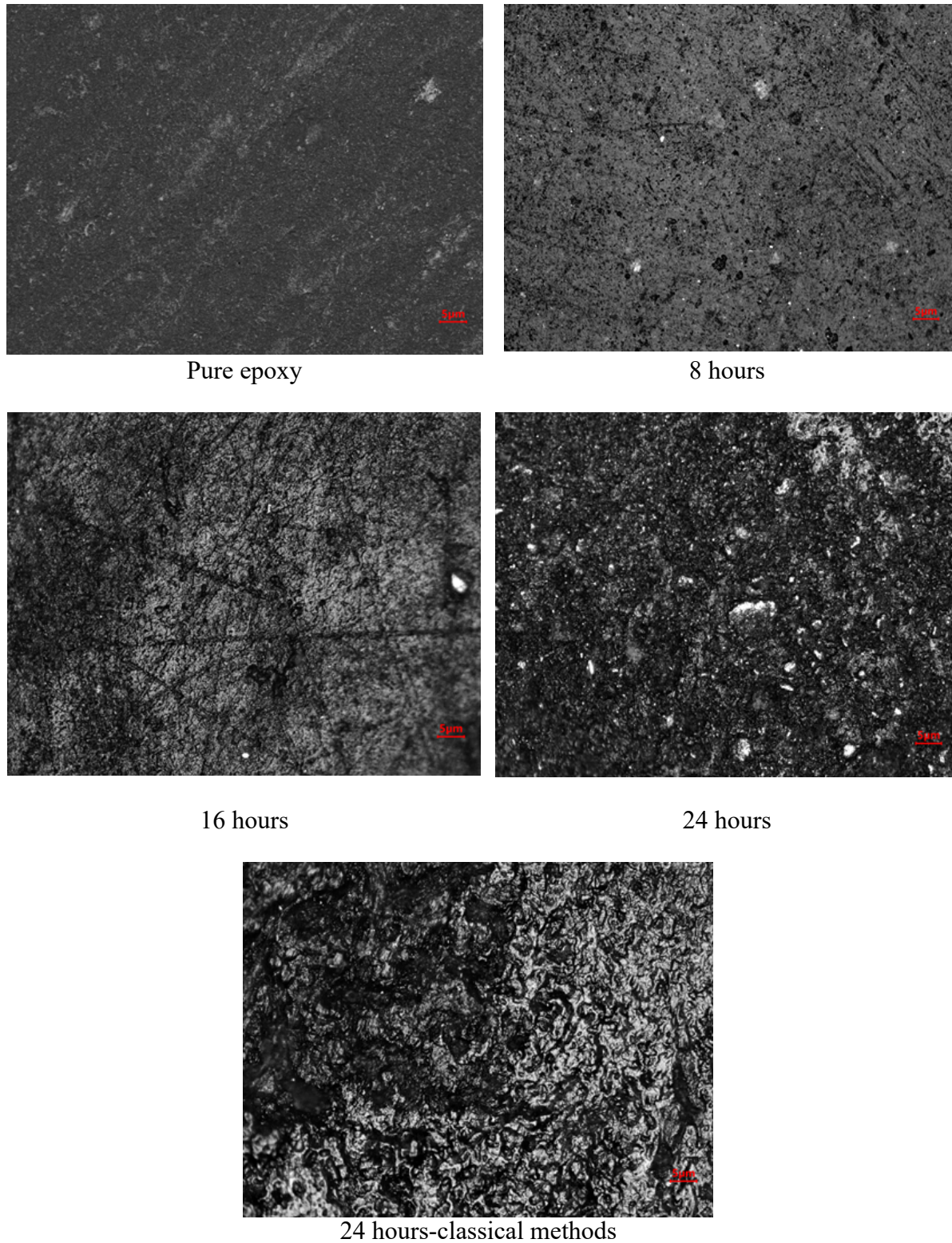


Fig. 3. Optical images of the given materials

#### 4. Conclusion

This study examines the W-Zn-Co-Y<sub>2</sub>O<sub>3</sub> alloy reinforced epoxy polymer composites in terms of Vicker hardness and density measurements. Component A and B were chosen as epoxy elements. The study indicates the second method may be chosen due to the highest Vicker hardness value and lower measured density values as compared to the reinforced composites. Furthermore, the

16 hours milled heavy tungsten alloy reinforced epoxy composites have the highest mechanical value. The utilization of the tungsten alloy as a reinforcement within the epoxy composites significantly enhanced their mechanical properties, thereby expanding the potential applications of composites in diverse industries, including aerospace, automotive, marine, and military sectors.

## References

- [1] Lu, Song, Jin-Yu Xu, Er-Lei Bai, Xin Luo., Effect of Particles with different Mechanical Properties on the Energy Dissipation Properties of Concrete. *Construction and Building Materials*, 144, 502-515, 2017.
- [2] Sakthivel, S.N., Kathuria, A., Singh, B., Utilization of Inferior Quality Aggregates in Asphalt Mixes: A Systematic Review. *Journal of Traffic and Transportation Engineering*, 9(5), 864-879, 2022.
- [3] Shahedan, Noor Fifinatasha, Mohd Mustafa., Potential of Geopolymer Coating for Lightweight Aggregate via Milling and Dipping Method: A Review. *European Journal of Materials Science and Engineering*, 7(2), 094–105, 2022.
- [4] Lim, T., Lee, J.H., Mun, J.H., Yang, K.H., Ju, S., Jeong, S.M., Enhancing Functionality of Epoxy–TiO<sub>2</sub>-Embedded High-Strength Lightweight Aggregates. *Polymers*, 12(10), 1-11, 2020.
- [5] Abutaha, F., Abdul Razak, H., Ibrahim, H.A., Effect of Coating Palm Oil Clinker Aggregate on the Engineering Properties of Normal Grade Concrete. *Coatings*, 7(10), 1-26, 2017.
- [6] Muñoz Jose F., Expanded Study on the effects of Aggregate Coating and Films on Concrete Performance, *Wisconsin highway research program*, 2007.
- [7] Muñoz, Jose F., M. Isabel Tejedor, Marc A. Anderson, and Steven M. Cramer., Detection of aggregate clay coatings and impacts on concrete. *ACI Materials Journal*, 107(4), 387-395, 2010.
- [8] Rajasekaran, S., Vasudevan, R., Paulraj, S., Reuse of Waste Plastics Coated Aggregates-Bitumen Mix Composite for Road Application - Green Method. *American Journal of Engineering Research*, 2(11), 1-13, 2013.
- [9] Alave, Y.B., Mahimkar, S.S., Patil, K.S., Gupta, J.J., Kazi, A., Experimental Investigation of Plastic Coated Aggregate. *International Journal of Engineering Research & Technology*, 9(3), 112-120, 2021.
- [10] Sharma, S.D., Sharm, A., Utilization of Waste Plastic in Flexible Pavement. *International Journal of Science and Research*, 8(5), 1545-1549, 2019.
- [11] Vasudevan, R.N.S.K., Nigam, S.K., Velkennedy, R., Sekar, A.R.C., Sundarakannan, B., Utilization of Waste Polymers for Flexible Pavement and Easy Disposal of Waste Polymers. *International Journal of Pavement Research and Technology*, 3, 34-42, 2010.
- [12] Harnadh K.L., A. M. N. Kashyap, K. M. Gupta, Experimental Investigation on Coarse Aggregates by using Waste Plastics & Polymers. *International Journal of Innovative Resesach in Engineering and Management*, 2(3), 19-23, 2015.


- [13] Dawale, S.A., Use of Waste Plastic Coated Aggregates in Bituminous Road Construction. *International Journal of Advancement in Engineering Technology, Management, and Applied Science*, 3(6), 118-126, 2016.
- [14] Gebre, Y., Lahmer, T., Müller, M., Wiegand, T., Osburg, A., & Tarekegn, A. G., Properties of Concrete with Coated Aggregates under different Loading Conditions. *Journal of Research in Engineering and Applied Sciences*, 8(1), 449-459, 2023.
- [15] Vahabi, Mir Yashar, Behzad Tahmouresi, Hossein Mosavi, and Siavash Fakhretaha Aval., Effect of pre-coating lightweight aggregates on the self-compacting concrete. *Structural Concrete*, 23(4), 2120-2131, 2023.
- [16] Popovics, J.S., Zemajtis, J., Shkolnik, I., A Study of Static and Dynamic Modulus of Elasticity of Concrete, *American Concrete Institute - Concrete Research Council*, Report 16, 2008.
- [17] Hansen, T. C., Recycled Aggregate and Recycled Aggregate Concrete. *Material and Structures*, 19, 201-246, 1986.
- [18] ASTM C 136 - Standard Test Method for Sieve Analysis of Fine and Coarse Aggregates, *ASTM International*, 2014.
- [19] Sikafloor®-161, Product Data Sheet, May 2019.
- [20] Epoxy T 19-32/1000, Product Data Sheet, February 2019.
- [21] BYK-C 8001, Polymeric Coupling Agent, Product Data Sheet, 2021.
- [22] EN 12390-4:2019: Testing Hardened Concrete - Part 4: Compressive Strength of Test Specimens, 2019.
- [23] ASTM C496-96: Standard Test Method for Splitting Tensile Strength of Cylindrical Concrete Specimens, *ASTM International*, 2017.
- [24] EN 12390-6:2009: Testing Hardened Concrete - Part 6: Tensile Splitting Strength of Test Specimens, 2009.
- [25] EN 12390-13:2021: Testing Hardened Concrete - Part 13: Determination of Secant Modulus of Elasticity in Compression, 2021.
- [26] ASTM C215-08: Standard Test Method for Fundamental Transverse, Longitudinal and Torsional Resonant Frequencies of Concrete Specimens, *ASTM International*, 2009.
- [27] Miura, T., Sato, K., Nakamura, H., The Role of Microcracking on the Compressive Strength and Stiffness of Cracked Concrete with different Crack Widths and Angles Evaluated by DIC. *Cement and Concrete Composites*, 114, 1-10, 2020.



## **Dendrobranchiata Chitin Deacetylation Degree and its Potency as Iron (III) Ion Adsorbent from Aqueous Solution**

Oluwashina Philips Gbenebor\*, Abimbola Patricia Idowu Popoola

Department of Chemical, Metallurgical and Materials Engineering, Tshwane University of Technology, Pretoria, South Africa

✉: [philipsogbenebor@gmail.com](mailto:philipsogbenebor@gmail.com), : 0000-0003-1693-4601\*, 0000-0003-4447-8551

Received: 25.08.2023, Revised: 02.11.2023, Accepted: 11.11.2023

### **Abstract**

*This research investigates the production of epoxy resin composites reinforced by the synthesized heavy tungsten alloys (W-7Zn-3Co-Y<sub>2</sub>O<sub>3</sub>). Y<sub>2</sub>O<sub>3</sub> is used for dispersion of the compound during the ball milling process. Laminating resin component A and hardened component B were used to produce polymer epoxy matrix. The tungsten heavy alloys reinforced epoxy composites were examined in terms of Vickers hardness, density measurement and microstructural characterization. The results indicate that the 16 hour-milled reinforced epoxy composites have the highest hardness value.*

**Keywords:** Tungsten alloys, mechanical alloying, and polymer epoxy composites

### **1. Introduction**

The quest to improve man's standard of living has engendered further creation and developments of industries which in turn, has hastened urbanization growth. Discharge of domestic wastes including those from industries' processing operations such as chemicals into water has made it harmful for human use. Organic pollutants have been found to be biodegraded by microbes to products useful to marine life [1]. Heavy metals such as lead (Pb), Nickel (Ni), copper (Cu), chromium (Cr), zinc (Zn), cadmium (Cd), arsenic (As), and iron (Fe), are harmful because of their non-biodegradable nature [2-3]. They mostly emanate in high concentrations from industries including mining, metal ore processing and electroplating industries as effluents [4]. Heavy metals have also been reported to gain access to the environment via soil erosion, rock weathering and pesticides applied to crops [5]. Waste water irrigation has been reported by Muchuweti et al. [6] to contaminate the soil which ends up poisoning the foods obtained from the plants that grow on the contaminated soil. Animals graze on these poisoned plants, drink from the polluted waters and thus have the heavy metals accumulated in their tissues. Marine lives breeding in the heavy metal-polluted water are not left out; all living things within a given ecosystem are contaminated along their cycles of food chain. Over the years, various techniques including precipitation, adsorption, oxidation, coagulation, flocculation and membrane filtration processes have been devised to eliminate these heavy metals from waste waters. Adsorption has been considered to be an economical technique as it offers the use of low cost adsorbents effective in treatment of water. In recent years, use of biopolymers as bio adsorbents has gained wide recognitions owing to their biodegradability, non-toxicity, accessibility and low cost of procurement. Among natural polymers, polysaccharide such as chitin has been confirmed an effective adsorbent. Second to cellulose in terms of natural polymer abundance, chitin is a linear polysaccharide of (1 → 4) linked units of N -acetyl-2- amino-2-deoxy- D – glucose [7]. While hydroxyl (OH) group exists on carbon C2 in cellulose, acetamide (RCONH<sub>2</sub>) group is formed on C2 in chitin; this gives a major structural difference between the two polysaccharides. The appreciable biodegradability and biocompatibility of chitin are responsible for its applications in



wound dressings where sponges [8] and suture threads [9] are being used. Its high thermal stability [10] enhances its suitability as a food packaging material. The degree of chitin acetylation (DA) is the percentage of acetyl (RC=O) groups present in chitin. Nam et al. [11] explains it as the ratio of *N*-acetylated group to *N*-de acetylated (amino, RNH<sub>2</sub>) groups. This parameter is often used to identify chitin and its derivative – chitosan. According to Kim, [12], a biopolymer is chitin when DA > 50 % while that lower than this value is classified as chitosan. Chitin has been used in the adsorption of Ar, Zn, Cu, Cd, Mn, Fe, Pb and Cr [13-17]. Jaafarzadeh et al. [13] synthesized chitin from shrimp shells by using 10% v/v hydrochloric acid (HCl) and sodium hydroxide (NaOH) as demineralization and deproteinization reagents respectively to adsorb Zn<sup>2+</sup> from aqueous solutions. Ease of Zn<sup>2+</sup> removal was ascribed to the increase in pH and chitin dose. Pulverized Bargi fish scales have been treated with 5% v/v HCl to remove calcium carbonate, CaCO<sub>3</sub> [18]. Chitin produced was used in removing Cr<sup>6+</sup> from aqueous solutions of potassium dichromate (K<sub>2</sub>Cr<sub>2</sub>O<sub>7</sub>) salt. The researchers concluded that the adsorption process was temperature and pH dependent as maximum adsorption capacity was attained at pH 6-8. In the works conducted by Forutan et al. [17], shells of pink shrimps were refluxed 7%v/v HCl and NaOH to extract chitin that would be suitable for the adsorption of Pb from lead stock solutions. Optimum conditions of pH, contact time, bioadsorption dosage and initial concentration of Pb were observed to be 9, 200 min, 5gr/L and 7.99ppm respectively. The best efficiency biosorption was discovered to be 99.7%. Chitosan has been processed from chitin sourced from crab shell for the removal of heavy metals from contaminated water [16]. Mineral such as CaCO<sub>3</sub> was eliminated from the crushed crab shells using 10% v/v HCl followed by protein removal with NaOH using the same concentration between 103-105 °C. zinc chloride (ZnCl<sub>2</sub>), Nickel chloride (NiCl<sub>2</sub>), iron (III) chloride (FeCl<sub>3</sub>), lead chloride (PbCl<sub>2</sub>), cadmium chloride (CdCl<sub>2</sub>), manganese (II) sulphate (MnSO<sub>4</sub>) and chromium (III) sulphate (Cr<sub>2</sub>(SO<sub>4</sub>)<sub>3</sub>) were used for chemical solutions. Chitosan was found to remove metal in the order Mn>Cd>Zn>Co>Ni>Fe>Pb>Cr. Concentrations of 2N HCl and 1N NaOH (at 80 °C) were used by Bhavani et al. [19] to process chitin from crab shells. Chitin produced was deacetylated by further reactions with 40% v/v NaOH at 110 °C for chitosan synthesis. The biopolymer served as a potential adsorbent of Cu<sup>2+</sup>, Zn<sup>2+</sup>, Cr<sup>6+</sup>, Cd<sup>2+</sup> and Pb<sup>2+</sup> from electroplating water waste. Results gathered from existing researches have shown that removal performance of chitin bioadsorbents is not similar for all heavy metals. This could be attributed to the different experimental techniques and conditions considered. This justifies the submissions of Bhavani et al. [19] who affirmed that high reactivity and selectivity of chitin towards compounds and metals are due to the presence of chemical reactive OH, RCONH<sub>2</sub> or RNH<sub>2</sub> groups in their polymer chains. The functionalities of these groups in chitin have been confirmed to be dependent on their source of origin as identified from previous works [20-22]. In this study, chitin isolated from prawn exoskeleton possessing different deacetylation degree (DDA) is characterized for its thermal and structural properties. In addition, the influence of chitin's varying DDA on its potency for Fe adsorption is investigated. Excess Fe in the body has been reported to cause osteoporosis as it prevents the differentiation and proliferation of osteoblasts [23]. Abnormal hepatic gluconeogenesis is another effect of Fe overload in the human body [24].

## 2. Materials and Methods

### 2.1. Chitin extraction

Exoskeletons of prawns were washed, dried and ground to 200 µm particle sizes. Demineralization was carried out by treating ground particles with 1M HCl until no evidence of CO<sub>2</sub> release was noticed. The demineralized samples were washed with distilled water to neutral pH, filtered and oven dried at 70 °C till it was completely dry. The demineralized powders were refluxed with 1 M NaOH at 100 °C for 1, 2, 3, 4 and 5 h to complete the deproteinization process.

Samples were washed, filtered and dried as earlier done for demineralized powders and chitin was finally obtained. In this study, C1, C2, C3, C4 and C5 designations are used to identify chitin extracted by deproteinizing for 1, 2, 3, 4 and 5 h respectively

## 2.2. Chitin characterizations

### 2.2.1. Fourier Transform Infrared Spectroscopy (FTIR)

Functional groups present in each chitin sample were identified using Nicolet 6700M spectrometer and processed at a resolution of  $4\text{ cm}^{-1}$ . Spectra were taken in the absorbance mode between  $500\text{--}4000\text{ cm}^{-1}$ . The degree of deacetylation, DDA was calculated using the formula in Eq. (1):

$$\text{DDA (\%)} = 100 - \text{DA} \quad (1)$$

Where DA is the degree of chitin acetylation which was calculated using Eq. (2): [20, 26]:

$$\text{DA} = \frac{A_{1650}}{A_{3450}} \times \frac{100}{1.33} \quad (2)$$

Amide I absorbance variation is represented by  $A_{1650}$ ; OH absorbance variation is represented by  $A_{3450}$ ; for full N-acetylated chitin ratio  $A_{1650}/A_{3450}$  is represented by the factor 1.33.

### 2.2.2. Thermogravimetric analysis (TGA)

Two milligram of each chitin sample was heated to  $750\text{ }^{\circ}\text{C}$  using TGA Q500 device at  $10\text{ }^{\circ}\text{C}/\text{min}$  heating rate. From the thermograms, temperatures at the commencement and conclusion of chitin decomposition were quantified.

### 2.2.3. X-Ray diffraction

A monochromatic Cu  $K\alpha$  radiation from a PANalytical device operated at  $40\text{ kV}$  and  $40\text{ mA}$ , was targeted at each chitin sample. The crystallinity, CrI was calculated from the diffractogram using Eq. (3) [27]:

$$\text{CrI (\%)} = [I_c / (I_c + I_a)] \times 100 \quad (3)$$

Where  $I_a$  and  $I_c$  are intensities of crystalline and amorphous peaks respectively  
Crystalline size of chitin samples were calculated using Eq. (4) [28]:

$$D_{hkl} = k\lambda / \beta \cos \theta \quad (4)$$

Value of K is assumed to maintain a constant value of 1. It stands for perfection of crystallite; incident radiation wave length ( $1.5406$ ) is represented by  $\lambda$ ;  $\beta$  (rad) represents the width of the crystalline peak at half height; and  $\theta$  (deg) stands for diffraction angle that corresponds to the crystalline peak.

### 2.2.4. Scanning Electron Microscopy (SEM)

Samples were coated with Au to enhance proper electrical conductivity which was scanned using an ASPEX 3020 model variable pressure SEM to identify the morphological features of chitin particles.

### 2.3. Preparation of Fe<sup>3+</sup> - rich solution and determination of chitin sorption capacity

A gram of iron (III) chloride (FeCl<sub>3</sub>) was dissolved in 1 L distilled water at room temperature. In this study, effects of pH (which ranged from 1-6) and contact time on Fe<sup>3+</sup> adsorption capacity of chitin samples were investigated. Chitin particles (0.5 g) was added to 100 ml FeCl<sub>3</sub> solution and continuously stirred at room temperature for 30, 60, 90, 120, 150 and 180 min, which were the contact times. To calculate the sorption capacity (q) of chitin, Eq. (5) [29] was used:

$$q \text{ (mg/g)} = [(C_o - C_i)/W] V \quad (5)$$

The initial and final concentrations of Fe<sup>3+</sup> in the solution is represented by C<sub>o</sub> and C<sub>i</sub> (mg/L) respectively; W represents the mass of chitin (g) and V stands for the volume of aqueous solution (L). As regards adsorption tests, chitin samples with the highest and lowest DDA were selected. An additional sample whose DDA value lied between these two was also chosen to make the total samples characterized for the adsorption tests three.

## 3. Results and Discussions

### 3.1. Functional groups and DDA

The FTIR spectra of C1, C2, C3, C4 and C5 are shown in Fig.1. Apart from different intensities displayed, pattern of all chitin samples are similar. Their existing functional groups are given in Table 1.

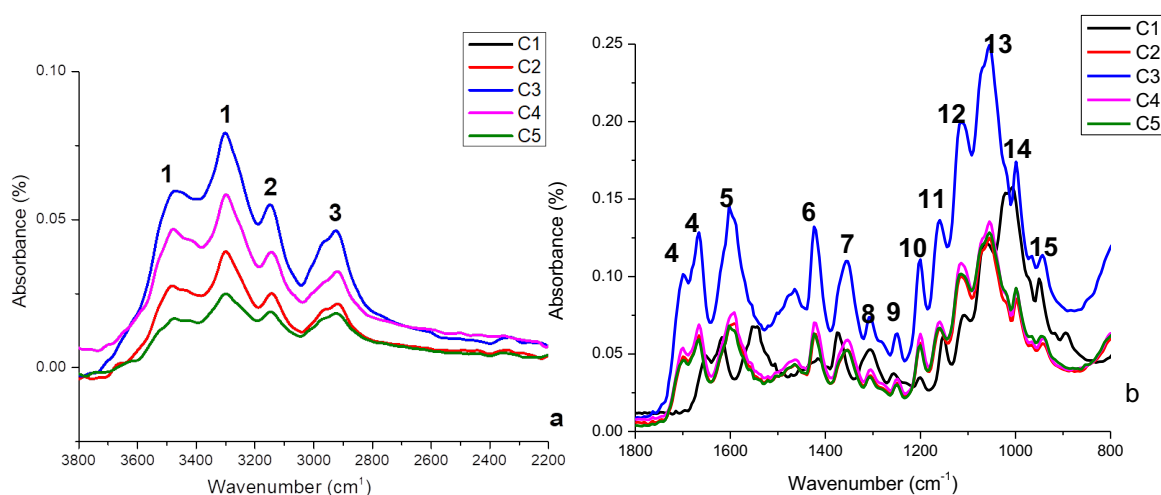


Fig. 1. FTIR spectra of chitin between (a) 3800 – 2200 cm<sup>-1</sup> and (b) 1600 – 800 cm<sup>-1</sup>

Maximum DDA (43.8 %) is obtained when chitin was deproteinized for 5 h (Fig.2) and this shows that gradual increase in reaction time between demineralized prawn exoskeleton and NaOH steadily removes *N*-acetyl groups in the glucopyranose units of the final product (chitin). This simultaneously raises the number of RNH<sub>2</sub> in the polymer chain. Result obtained from this study shows that sufficient reaction time during deproteinization engenders the instability of the bond in RCONH<sub>2</sub>. Also, this result informs that NaOH concentration alone will not influence DDA as earlier demonstrated in the investigation of Gbenezor et al. [20]. Aranaz et al. [30] reported that there is usually a reduction in the resistance of RCONH<sub>2</sub> on the C2-C3 substituent arrangement of the glucopyranose chitin ring. This could have triggered hydrolysis of the group (RCONH<sub>2</sub>) by virtue of increasing deproteinization time.

Table 1. Functional groups of prawn chitin

S/N	Functional groups	Wavenumber (cm <sup>-1</sup> )
1	OH stretching	3443-3487; 3259-3298
2	NH stretching	3096-3149
3	Symmetric CH <sub>3</sub> stretching and asymmetric CH <sub>2</sub> stretching	2925
4	C=O secondary amide stretch (Amide I)	1661, 1626
5	NH bend, CN stretch (Amide II)	1559
6	CH <sub>2</sub> bending and CH <sub>3</sub> deformation	1416
7	CH bending and CH <sub>3</sub> symmetric deformation	1379
8	CH <sub>2</sub> wagging (Amide III)	1312
9	Asymmetric bridge oxygen stretching	1157
10	Asymmetric in -phase ring stretching mode	1117
11	C-O-C asymmetric stretch in phase ring	1074
12	CO stretching	1028
13	CH <sub>3</sub> wagging along chain	933
14	CH stretching (saccharide rings)	897
15	NH out-plane bending	750

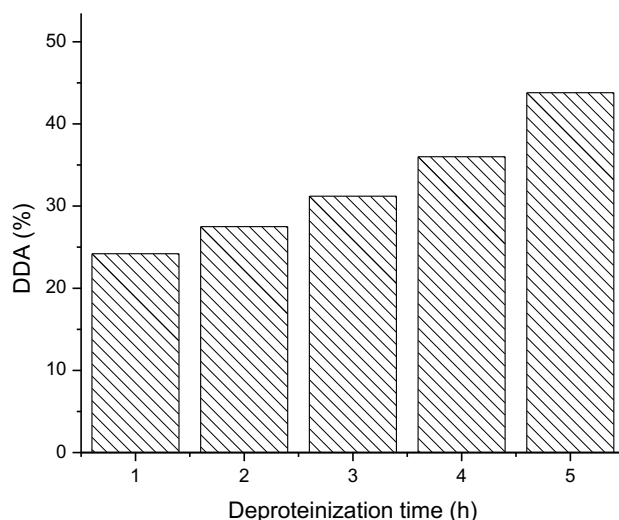


Fig. 2. DDA of chitin as a function of deproteinization time

### 3.2. Thermal response and chitin content

There exist two stages of decomposition (Fig. 3) – the first, which is a minor step, occurs between 50 – 110 °C and this represents the evaporation of moisture content in chitin. The second decomposition stage is a major step which commences between 161 and 309 °C ( $T_{\text{onset}}$ ) and ends ( $T_{\text{finish}}$ ) between 260 and 438 °C. This major decomposition represents the existence of chitin, which is similar to the findings of Gbenebor et al. [20]. One of or the combination of denaturation, depolymerization and degradation according to Juarez de la Rosa et al. [31] exist(s) within this temperature range. Here, chitin's structure becomes devoid of CH<sub>3</sub>-CH<sub>2</sub> in aliphatic compounds;



decompositions of C=O and NH in Amides I and II proceeds after and finally, C-O-C in the saccharide separates from chitin. [27]. The values of  $T_{\text{onset}}$ ,  $T_{\text{finish}}$ , contents of moisture, chitin and residue are displayed in Table 2. In this study, thermal stability is defined as the minimum temperature at which chitin molecular bonds begin to disintegrate (this is determined by comparing magnitudes of  $T_{\text{onset}}$ ). It is noticed in this study that thermal stability of chitin sample reduces with increase in deproteinization time as the maximum  $T_{\text{onset}}$  is recorded at 309 °C for C1 while C5 maintains the least  $T_{\text{onset}}$  at 161 °C. Presence of the most thermally stable *N*-acetyl (GlcNAc) units in C1 could be responsible for this. Kahdestani et al. [32] characterized chitosan for TGA and observed its  $T_{\text{onset}}$  to attain a magnitude of 195 °C while Nam et al. [11] reported chitosan samples to exhibit  $T_{\text{onset}}$  values between 164 and 174 °C. This shows that C5 will possess features close to chitosan. It can also be confirmed from this study that residue and chitin contents may not be dependent on deproteinization time.

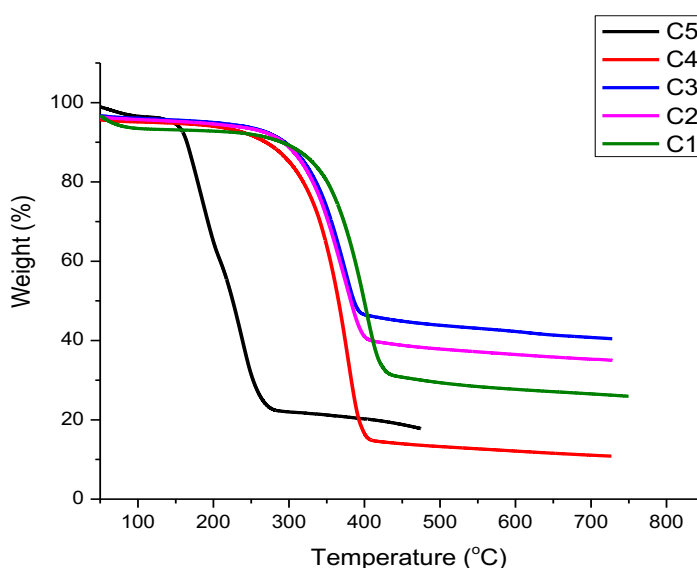


Fig. 3. TGA of isolated chitin after 1, 2, 3, 4 and 5 h deproteinization

Table 2. TGA parameters of isolated chitin after 1, 2, 3, 4 and 5 h deproteinization

S/N	Chitin	$T_{\text{onset}}$ (°C)	$T_{\text{finish}}$ (°C)	Chi mass loss (%)	Moisture (%)	Residue (%)
1	C1	309	438	61.1	8.9	30.0
2	C2	294	401	57.0	7.0	36.0
3	C3	284	391	48.7	6.3	45.0
4	C4	278	405	77.0	8.4	14.6
5	C5	161	260	72.7	5.2	22.1

### 3.3. Crystalline properties

X-ray diffraction of chitin samples are shown in Fig. 4. All samples follow similar patterns but with different intensities, indicating the effect of prolonged NaOH reactions. A major peak (19.5°) corresponds to (110) while other four peaks of 9.8, 20.6, 23.4 and 26.5° diffracting on (020), (120), (130) and (013) are observed. Increasing deproteinization time culminates in reduction in peak intensities of each sample. The CrI of C1 is 84.5% while 81.3, 78.3, 73.8 and 67.8% are calculated for C2, C3, C4 and C5 respectively. This implies that the structural stability

of chain decreases as a result of gradual removal of *N*-acetyl groups, which eventually scales down its crystallinity. The crystallite sizes ( $D_{hkl}$ ) of chitin samples processed from varying deproteinization times are illustrated in Table 3. Information from the results imply that the lower the average crystallite size, the less crystalline the polysaccharide. The lowest CrI processed by C5 could be responsible for its least response to thermal energy as discussed in Fig. 3.

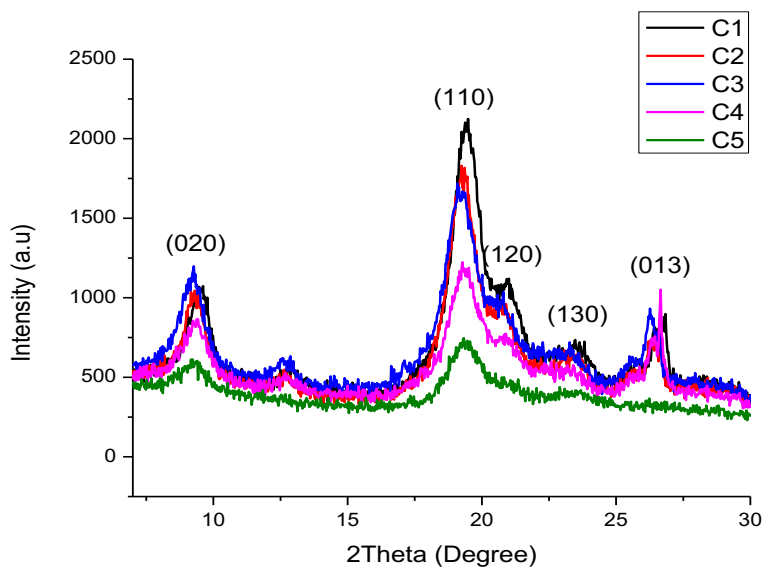


Fig. 4. XRD of isolated chitin after 1, 2, 3, 4 and 5 h deproteinization

Table 3. Crystallite properties and crystallinity of isolated chitin after 1, 2, 3, 4 and 5 h deproteinization

S/N	Chitin	$D_{020}$ (Å)	$D_{110}$ (Å)	$D_{120}$ (Å)	$D_{130}$ (Å)	$D_{130}$ (Å)	Average (Å)	CrI (%)
1	C1	0.6004	1.1821	0.1792	83.874	0.0386	17.170	84.5
2	C2	1.3823	1.2483	1.5558	0.6918	1.3988	1.2554	81.3
3	C3	0.9757	1.3594	0.4997	0.2748	2.6899	1.1599	78.3
4	C4	0.7438	1.816	0.4973	0.0348	0.2864	0.6767	73.8
5	C5	0.4285	0.943	--	0.0505	--	0.4707	67.8

### 3.4. Morphology

The morphology of C1 as presented in Fig. 5a shows a plate-like fibrillar form. This fibrillar nature is also processed by C2, but with a reduced geometry (Fig. 5b). It is noticed in this study that prolonged deproteinization time makes the surface of chitin particles look shiny/bleached. This could be an indication of gradual reduction of nitrogen and carbon in C=O and CN (from Amides I and II). There has been steady reduction in size of these plate-like fibrils as deproteinization time was carried out for 3, 4 and 5 h (Fig. 5c-e).

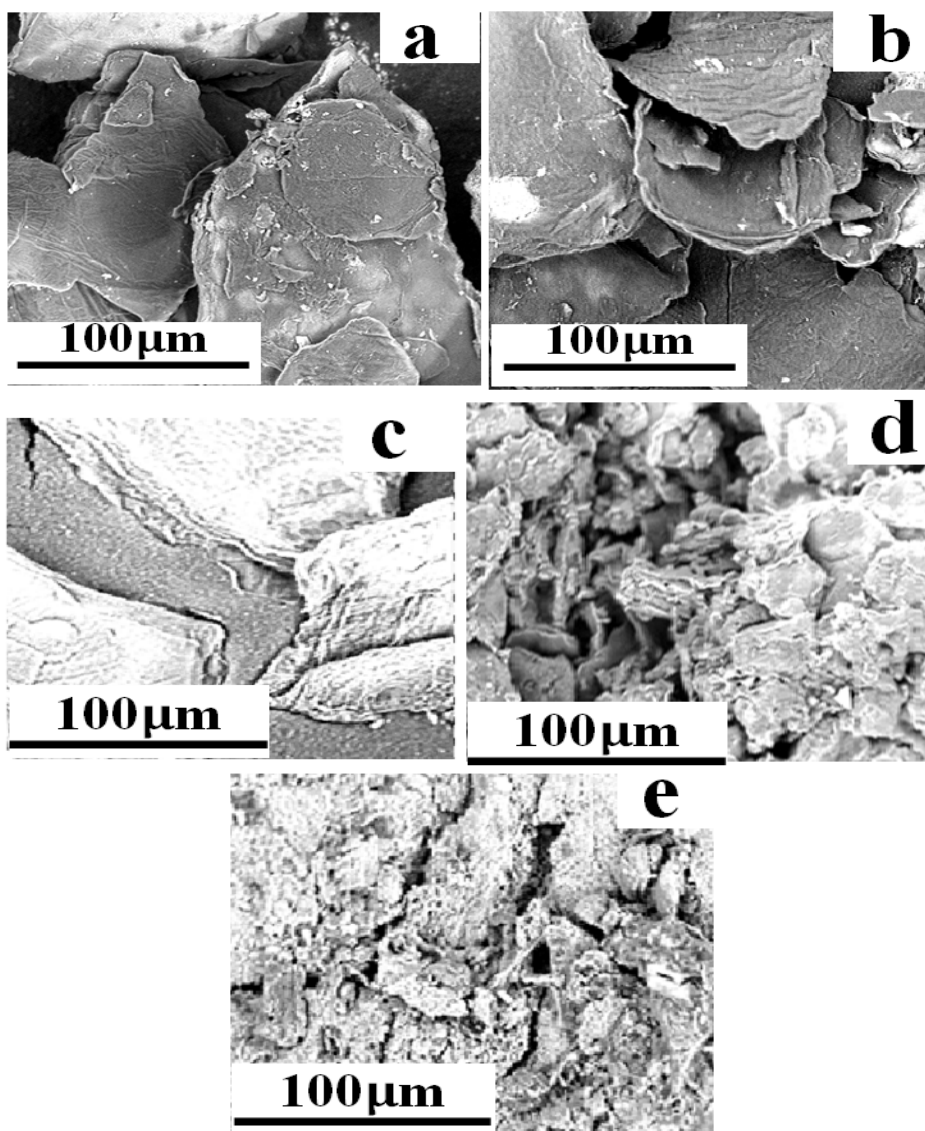


Fig. 5. SEM of chitin (a) C1 (b) C2 (c) C3 (d) C4 (e) C5

### 3.5. Effect of contact time on $\text{Fe}^{3+}$ sorption capacity of chitin

The concentration of  $\text{Fe}^{3+}$  that can be adsorbed on to chitin samples (C1, C3 and C5) by virtue of chitin -  $\text{Fe}^{3+}$  contact time between 30 – 180 min was investigated at room temperature, pH 5 and 150 rpm stirring speed. It is evident from Fig. 6 that for each chitin, the amount of  $\text{Fe}^{3+}$  adsorbed increases from 30 min and reaches a maximum value at 120 min. Within these periods, it can be reported that chitin provides favourable surface areas for  $\text{Fe}^{3+}$  adsorption. Beyond 120 min contact time, adsorption capacities of each chitin sample gradually drop and this can be attributed to saturation of surfaces occupied by  $\text{Fe}^{3+}$ . This is similar to the investigation of Gokila et al. [33] who confirmed that the decline in adsorption capacity of chitosan-alginate-nanocomposite on  $\text{Cr}^{6+}$  after 300 min was ascribed to the exhaustion of adsorption sites as there were no more unsaturated surfaces for adsorption. Chitosan has been used as adsorbent on Pb and Ni [34], After 180 min, the amount of  $\text{Pb}^{2+}$  and  $\text{Ni}^{2+}$  remained constant. The maximum content of  $\text{NH}_2$  groups as depicted by the highest DDA (43.8 %) may be responsible for the best adsorption performance displayed by C5. Its ability to allow aqueous solutions penetrate through its structure owing to its least value of Crl (67.8 %) may also be a determining factor for its best adsorption display. The Crl and DDA of C3 are 78.3 % and 31.5 % respectively; this implies there exists 31.5 % of  $\text{NH}_2$  groups compared to C1 that has 24.2 %. It (C3) will still give room

for aqueous solution penetration into its structure than C1 whose  $C_{rl}$  is 84.5 %. This could be the reason why the  $Fe^{3+}$  adsorption feature of C3 > C1.

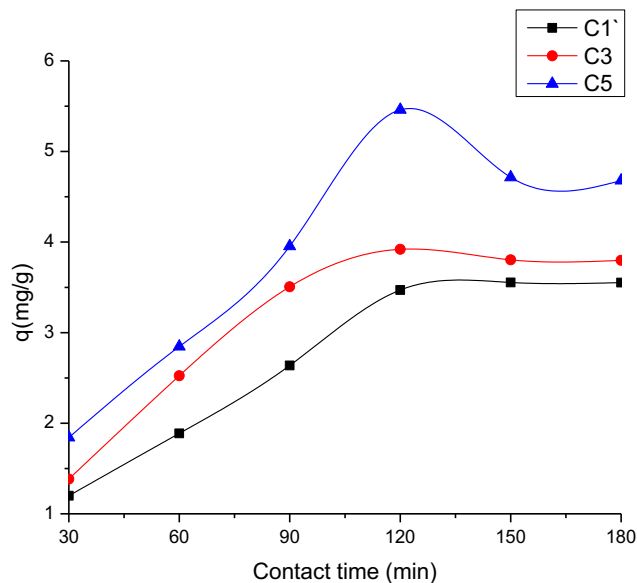


Fig. 6. Effect of contact time on  $Fe^{3+}$  adsorption capacity of C1, C3 and C5

### 3.6. Effect on pH on $Fe^{3+}$ sorption capacity of chitin

Fig. 7 shows the effect of pH on the adsorption of  $Fe^{3+}$  by chitin samples (C1, C3 and C5). Results were taken for pH values ranging between 1 and 6 at constant stirring speed (150 rpm) and contact time of 120 min at room temperature. The pH has been confirmed to an important parameter that influences ionization degree of metal, solubility of metal ions and surface features of adsorbent [19, 35]. Each sample display improved  $Fe^{3+}$  adsorption performance as the pH gradually increases to a maximum sorption coefficient at pH 5. At lower pH, the solution is acidic and there will be electrostatic repulsion between  $H^+$  and  $Fe^{3+}$  which compete for bonding sites on chitin surface. In addition,  $NH_2$  groups in chitin are protonated by the high concentrations of  $H^+$  in the acidic solution; this further engenders repulsion of  $Fe^{3+}$ . As the pH values increase, the concentration of  $H^+$  in the solution decreases as well as  $NH_2$  protonation. This elevates the sorption coefficient of each chitin sample as more binding surface is increased and electrostatic repulsion is limited [36-37]. Although all chitin samples display adsorption potency for  $Fe^{3+}$ , C5 shows the best performance and this can be attributed to the highest DDA it possesses. It implies that the sample (C5) has the highest density of free  $NH_2$  groups that culminates in creation of active adsorption sites. This is a feature that makes chitosan a better heavy metal adsorbent than chitin [38]. Beyond pH5, adsorption capacities of C1, C3 and C5 drop as a result of a likelihood of a metal hydroxide ( $Fe(OH)_3$  in this case) formed which could have prevented the metal ions from contacting chitin active site [39].

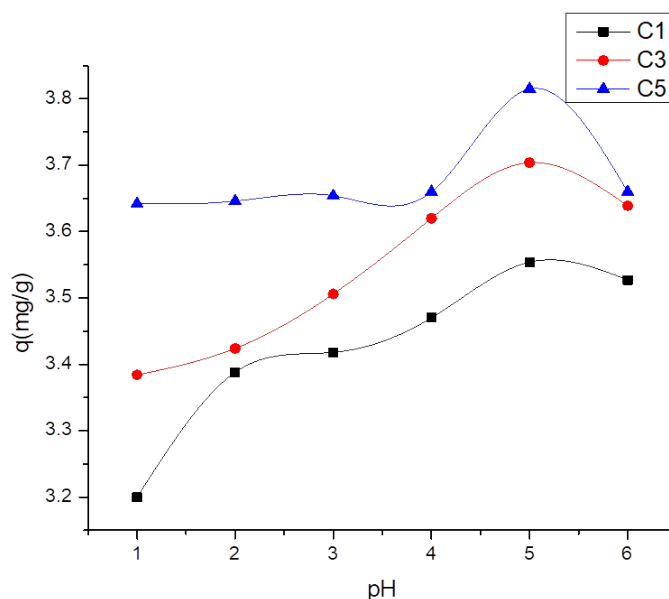


Fig.7. Effect of pH on  $\text{Fe}^{3+}$  adsorption capacity of C1, C3 and C5

#### 4. Conclusions

Influence of deproteinization time on the properties of prawn chitin has been successfully studied. Thermal stability of chitin decreases as the time allowed for deproteinization increases. More time is allowed for the glycosidic bonds in chitin to disintegrate and on the 5th hour, the thermal characteristics of the sample is comparable to that of chitosan as this is justified by its lowest DDA value of 43.8 %. There is also a gradual decrease in chitin's crystallinity from 84.5 to 67.8 % after deproteinization from 1 to 5 h. This implies that the bond strength in chitin can be altered as more of  $\text{RNH}_2$  groups are formed during deacetylation. Results from this study have shown that  $\text{RC=O}$  groups are responsible for chitin strength and will thus play important role in its thermal and structural properties. Sorption capacity of selected chitin for  $\text{Fe}^{3+}$  offers its best performance at pH 5 and 120 min contact time at room temperature and constant stirring speed (150 rpm). It can be affirmed that existence of more  $\text{RNH}_2$  in chitin improves the adsorption potency of chitin and that is why in terms of  $\text{Fe}^{3+}$  adsorption performance, C5 (DDA 43.8 %) > C3 (DDA 31.5 %) > C1 (DDA 24.2 %). This study has been able to establish that apart from reagent type, temperature and concentration considered during deproteinization, reaction time is also a notable parameter that can affect the structure and performance of chitin. Further studies are ongoing with the aim of considering the kinetics and mechanisms involved in the interactions between chitin adsorbents (of different physical and structural modifications) and other heavy metals including Fe.

#### References

- [1] Sankhla, M.S., Kumari, M., Nandan, M., Kumar, R. and Agrawal, P., Heavy Metals Contamination in Water and their Hazardous Effect on Human Health- A Review. *International Journal of Current Microbiology and Applied Sciences*, 5(10), 759-766, 2016.
- [2] Verma, R. and Dwivedi, P., Heavy Metal Water Pollution- A Case Study. *Recent Research in Science and Technology*, 5(5), 98-99, 2013.

- [3] Jaishankar, M., Tseten, T., Anbalagan, N., Mathew, B.B. and Beeregowda, K.N., Toxicity, Mechanism and Health Effects of Some Heavy Metals. *Interdisciplinary Toxicology*, 7(20), 60-72, 2014.
- [4] Anastopoulos, I., Bhatnagar, A., Bikiaris, D.N. and Kyzas, G.Z., Chitin Adsorbents for Toxic metals: A Review. *International Journal of Material Sciences*, 18(114), 1-111, 2017.
- [5] Morais S, Costa F.G, and Pereira, M.L., Heavy Metals and Human Health, Environmental health – emerging issues and practice, Chapter 10, 227–246, 2012.
- [6] Muchuweti, M., Birketi, J.W., Chinyanga, E., Zvauya, R., Scrimshaw, M.D. and Lester, J.N., Heavy Metal Contents of Vegetables Irrigated with Mixture of Wastewater and Sewage Sludge in Zimbabwe: Implications for Human Health. *Agriculture, Ecosystems & Environment*, 112, 41-48, 2006.
- [7] Zhao, Y., Ju, W.T., Jo, G.H., Jung, W.J. and Park, R.D., Perspectives of Chitin Deacetylase Research. *Biothechnology of Polymers*, 131-144, 2011.
- [8] Li, S., Li, X., Zheng, L., Ruiz-Hitzky, E., Xu, . and Wang, X., MXene-Enhanced Chitin Composite Sponges with Antibacterial and Hemostatic Activity for Wound Healing. *Advanced Health Care Materials*, 1-6, 2022.
- [9] Odili, C.C., Ilomuanya, M.O., Sekunowo, O.I., Gbenebor, O.P. and Adeosun, S.O., Knot Strength and Antimicrobial Evaluations of Partially Absorbable Suture. *Progress in Biomaterials*, 12, 51–59, 2023.
- [10] Gbenebor, O.P., Adeosun, S.O., Adegbite, A.A. and Akinwande A., Organic and Mineral Acid Demineralizations: Effects on *Crangon* and *Liocarcinus Vernalis* –Sourced Biopolymer Yield and Properties. *Journal of Taibah University for Science*, 12(6), 837-845, 2018.
- [11] Nam, Y.S., Park, W.H., Ihm, D. and Hudson, S.M., Effect of the Degree of Deacetylation on the Thermal Decomposition of Chitin and Chitosan Nanofibers. *Carbohydrate Polymers*. 80, 291-295, 2011.
- [12] Kim, S., Chitin, Chitosan, Oligosaccharides and their Derivatives; Biological and their Bpplications. *CRC Press, Taylor & Francis Group*, 3-633, 2011.
- [13] Jaafarzadeh, N., Mengelizadeh, N., Takdastan, A., Heidari-Farsani, M. and Niknam, N., Adsorption of Zn(II) from Aqueous Solution by using Chitin Extraction from Crustaceous Shell. *Journal of Advances in Environmental Health Research*, 2, 110–119, 2014.
- [14] Jaafarzadeh, N., Mengelizadeh, N., Takdastan, A., Farsani, M.H., Niknam, N., Aalipour, M., Hadei, M. and Bahrami, P., Biosorption of Heavy Metals from Aqueous Solutions onto Chitin. *International Journal of Environmental Health Engineering*, 4, 1–7, 2015.
- [15] Kocer, N.N., Uslu, G. and Cuci, Y., The adsorption of Zn(II) Ions onto Chitin: Determination of Equilibrium, Kinetic and Thermodynamic Parameters. *Adsorption Science & Technology*, 2 (26), 333–344, 2008.
- [16] Rana, M.M., Removal of Heavy Metal from Contaminated Water by Biopolymer Crab Chitosan. *Journal of Applied Sciences*, 9(15), 2762 - 2769, 2009.

- [17] Forutan, R., Ehsandoost, E., Hadipour, S., Mobaraki, Z., Saleki, M. and Mohebbi<sup>3</sup>, G., Kinetic and Equilibrium Studies on the Adsorption of Lead by the Chitin of Pink Shrimp (*Solenocera melantho*). *Entomology and Applied Science*, 33(3), 20-26, 2016.
- [18] Otuonye, U.C., Barminas, J.T., Magomya<sup>1</sup>, A.M., Kamba, E.A. and Andrew, C., Removal of Chromium (VI) as a Heavy Metal from Aqueous Solution using Chitin Obtained from Bargi Fish (*Heterotis Miloticus*) scale. *Sci-Afric Journal of Scientific Issues, Research and Essays*, 2 (3), 128-131, 2014.
- [19] Bhavani, K., Roshan, B.E., Selvakumar, S. and Shenbagarathai, R., Chitosan– A low Cost Adsorbent for Electroplating Waste Water Treatment. *Journal of Bioremediation & Biodegradation*, 7(3), 1-6, 2016.
- [20] Gbenebor, O.P., Adeosun, S.O., Lawal, G.I., Jun, S. and Olaleye, S.A., Acetylation, Crystalline and Morphological Properties of Structural Polysaccharide from Shrimp Exoskeleton. *Engineering Science and Technology, an International Journal*, 20, 1155–1165, 2017a.
- [21] Gbenebor, O.P., Akpan, E.I. and Adeosun, S.O., Thermal, Structural and Acetylation Behavior of Snail and Periwinkle Shells Chitin. *Progress in Biomaterials*, 6, 97–111, 2017b.
- [22] Akpan, E.I., Gbenebor, O.P. and Adeosun, S.O., Synthesis and Characterization of Chitin from Periwinkle (*Tympanotonus Fusatus* (L.)) and Snail (*Lissachatina Fulica* (Bowdich)) Shells. *International Journal of Biological Macromolecules*, **106**, 1080-1088, 2018.
- [23] Yamasaki, K. and Hagiwara, H., *Excess Iron Inhibits Osteoblast Metabolism*. *Toxicology Letters*, 191(2-3), 211-215, 2009.
- [24] Lee, H.J., Choi, J.S., Lee, H.J., Kim, W.H., Park, S.L. and Song, J., Effects of Excess Iron on Oxidative Stress and Gluconogenesis through Hecpidin During Mitochondrial Dysfunction. *The Journal of Nutritional Biochemistry*, 26(12), 414-1423, 2015.
- [25] Lee, H.J., Choi, J.S., Lee, H.J., Kim, W.H., Park, S.L. and Song, J., Effects of Excess Iron on Oxidative Stress and Gluconogenesis through Hecpidin During Mitochondrial Dysfunction. *The Journal of Nutritional Biochemistry*, 26(12), 414-1423, 2015.
- [26] Kaya, M., Seyyar, O., Baran, T. and Turkes, T., Bat Guano as New and Attractive Chitin and Chitosan Source.. *Frontiers in Zoology*. 11, 1-1-10, 2014.
- [27] Juarez-de la Rosa, B.A., Quintana, P., Ardisson, P.L., Ya'nez-Limon, J.M. and Alvarado-Gil, J.J., Effects of Thermal Treatments on the Structure of Two Black Coral Species Chitinous Exoskeleton. *Journal of Materials Science*, 47, 990–998, 2012.
- [28] Al-Sagheer, F.A., Al-Sughayer, M.A., Muslim, S. and Elsabee, M.Z., Extraction and Characterization of Chitin and Chitosan from Marine Sources in Arabian Gulf. *Carbohydrate Polymers*, 77, 410–419, 2009.

- [29] Jaafarzadeh, N., Mengelizadeh, N. and Hormozinejad, M., Adsorption of Zn (II) Ion from Aqueous Solution by using Chitin Extracted from Shrimp Shells. *Jentashapir Journal of Health Research*, 5(3), 133 – 138, 2014.
- [30] Aranaz, I. , Mengíbar, M., Harris, R., Paños, I. Miralles, B., Acosta, N., Galed, G. and Heras, A., Functional Characterization of Chitin and Chitosan. *Current Chemical Biology*. 3, 203–230, 2009.
- [31] Juárez-de la Rosa, B.A., Crespo, J.M., Owen, Q., González-Gómez, W.S., Yañez-Limón, J.M., and Alvarado-Gil, J.J., Thermal Analysis and Structural Characterization of Chitinous Exoskeleton from Two Marine Invertebrates. *Thermochimica Acta*. 610, 16–22, 2015.
- [32] Kahdestani, S.A., Shahriari, M.H. and Abdouss, M., Synthesis and Characterization of Chitosan Nanoparticles Containing Teicoplanin using Sol–Gel. *Polymer Bulletin*, 78, 1133–1148, 2021.
- [33] Gokila, S., Gomathi, T., Sudha, P.N. and Anil, S., Removal of the Heavy Metal ion Chromium(VI) using Chitosan and Alginate Nanocomposites., *International Journal of Biological Macromolecules*, 104, 1459-1468, 2017.
- [34] Akinyeye, O.J., Ibigbam, T.B. and Odeja, O., Effect of Chitosan Powder Prepared from Snail Shells to Remove Lead (II) Ion and Nickel (II) Ion from Aqueous Solution and Its Adsorption Isotherm Model. *American Journal of Applied Chemistry*, 4(4), 146-156, 2016.
- [35] Zhang, L., Zeng, Y. and Cheng, C., Removal of Heavy Metal ions using Chitosan and Modified Chitosan: A Review. *Journal of Molecular Liquids*, 214, 175-191, 2016.
- [36] Jeon, C. and Holl, W.H., Chemical Modification of Chitosan and Equilibrium Study for Mercury Ion Removal. *Water Research*, 37, 4770 – 4780, 2003.
- [37] Benavent, M., Moreno, L. and Martinez, J., Sorption of Heavy Metals from Gold mining Wastewater using Chitosan. *Journal of the Taiwan Institute of Chemical Engineers*, 42, 976-988, 2011.
- [38] Ngah, W.W., Teon, L.C. and Hanafiah, M.A.K.M., Adsorption of Dyes and Heavy Metal Ions by Chitosan Composites: A Review. *Carbohydrate Polymers*, 83, 1446–1456, 2011.
- [39] Ahmadi, M., Rahmani, H., Ramavand, B. and Kakavandi, B., Removal of Nitrate from Aqueous Solution using Activated Carbon Modified with Fenton reagents. *Desalination and Water Treatment*, 76, 265–275, 2017.





## Large Deformation Analysis of Hyperelastic Continuum with Hexahedral Adaptive Finite Elements

Mustafa Tekin <sup>a</sup>, Bahadır Alyavuz <sup>b\*</sup>

<sup>a</sup> Gazi University, Graduate School of Natural and Applied Sciences, Department of Civil Engineering, Ankara, Türkiye

<sup>b</sup> Gazi University, Faculty of Engineering, Department of Civil Engineering, Ankara, Türkiye

✉: [mustafatekincsb@gmail.com](mailto:mustafatekincsb@gmail.com)<sup>a</sup>, [balyavuz@gazi.edu.tr](mailto:balyavuz@gazi.edu.tr)<sup>b</sup> : 0000-0003-2130-6407<sup>a</sup>, 0000-0003-4643-4368<sup>b</sup>

Received: 06.10.2023, Revised: 12.12.2023, Accepted: 23.12.2023

### Abstract

The use of hyperelastic materials capable of large deformations, such as elastomeric bearings used to reduce seismic effects, is quite common in civil engineering. Such environments are, in most cases, addressed by numerical solution techniques such as the finite element method. In case of large deformations, nonlinear analysis is used in the solution. In the study presented here, large deformations of a hyperelastic continuum expressed by the Mooney-Rivlin material model are calculated using hexahedral adaptive finite elements. A code was written in MATLAB using the total Lagrangian formulation for the nonlinear adaptive finite element solution. Comparisons were made with Abaqus software to check the consistency of the results obtained from this program. It has been observed that local refinements in the adaptive element mesh occur in the regions where they are needed. Considering the variation of maximum displacement and maximum stress with the number of elements, it has been observed that mesh refinement creates a convergent solution.

**Keywords:** Hyperelasticity, adaptive finite element method, hexahedral elements.

### 1. Introduction

Hyperelasticity is used for materials that are nonlinear and capable of large deformation, where the constitutive equation is derived from an elastic potential. These types of materials are frequently encountered in the field of civil engineering as well as in various sectors. One of the important area of use is elastomeric bearings used for reducing seismic forces on structures. These environments, which involve large deformation of hyperelastic materials, are in most cases handled with numerical solution techniques such as finite element method (FEM).

Regarding the solutions obtained from FEM, how the problem geometry is divided into finite elements is an important factor affecting the solution. Results generally become more accurate as the finite element size decreases. The process of dividing the elements into smaller elements is referred as mesh refinement. As a result of mesh refinement, the solution time increases as the number of elements increases. Therefore, an effective solution can be achieved by refining the mesh only where necessary. At this point, mesh refinement can be done in user-defined regions, or an automatical mesh refinement strategy based on a particular predefined refinement criterion can be used. The second one can be called adaptive mesh refinement. The method turns into adaptive finite element analysis with a criterion that uses the results obtained from finite element analysis.

In modeling a three-dimensional geometry, tetrahedral elements (tetrahedrons), which consist of four triangular faces, and hexahedral elements (hexahedrons), which consist of six faces, are commonly used. Tetrahedrons enable the creation of an element mesh that better represents



geometry boundaries and enables easier transition from small elements to large elements, especially for non-uniform geometries and adaptive solutions. On the other hand, using hexahedrons shortens the calculation time by requiring fewer elements and provides more accurate solutions due to the additional terms in the shape functions used for interpolation [1]. Linear tetrahedral elements also exhibit "volumetric locking" and "shear locking" problems due to their more rigid behavior, so hexahedral finite elements are preferred [2].

Creating a finite element mesh using hexahedral elements can be done by several different methods. The element mesh created by dividing the geometry into uniformly distributed hexahedral elements is called a regular element mesh. The problem geometry is divided into finite elements using a grid with equal number of points on opposite edges [3]. A regular element mesh is a fast option in cases where there are no curvilinear boundaries. Using an unequal number of points on opposite edges makes the distribution of hexahedral elements irregular. Irregular finite element mesh, which provides a more flexible option in dividing the geometry into elements, is an element mesh that must be created in complex geometries with curvilinear surfaces. This type of finite element mesh can be created by direct and indirect methods. Dividing [4] or combining [5] tetrahedron elements created as the initial element mesh is an indirect method for creating hexahedral elements. With grid-based methods, which are direct methods, a regular hexahedral grid is first placed in the geometry, and then the gaps between the grid and the geometry boundary are filled with hexahedral elements [3]. Direct and indirect methods such as sweeping [6,7], advancing front [1, 8], and subdivision [9] are other methods that can be used to create hexahedral element meshes in complex geometries.

In a mesh containing hexahedral elements, dividing an element into smaller elements to achieve regional refinement is a frequently used method. However, a discontinuity occurs between the divided element and neighboring elements. Therefore, neighboring elements must be divided in addition to the divided element to ensure continuity. These elements, which provide continuity in the hexahedral element mesh refinement, are defined as transition elements [10]. Hexahedron partitioning types and shapes of transition elements for different local refinement strategies have been shown in various studies [10-12].

The adaptive element mesh can be created using geometric features of the problem or using a calculated indicator [13]. In geometric adaptive methods, refinement is done through points, edges, and surfaces on the element depending on the characteristics of the problem geometry [14]. Geometric features such as surface curvatures, sharp-edged regions, and boundaries, can be used to create a geometric adaptive element mesh [14-19]. In methods based on an indicator, an error estimator is calculated at each element using the initial mesh [20-24]. Refinement or coarsening is made in the elements to create an evenly distributed error estimate in the mesh. Variation of parameters such as stress, strain, or temperature obtained from an initial FEM solution can also be used to create an adaptive finite element mesh [25, 26].

Although the finite element method was initially created to solve linear behavior, it was expanded over time to model the nonlinear behavior of hyperelastic materials, including compressibility [27-29] and incompressibility [30-32]. In related studies, triangular elements [33] and quadrilateral elements [34, 35] for two dimensional problems, tetrahedral elements [36] and hexahedral [31,32,37,38,39] elements in three-dimensional problems were frequently used. In order to obtain more realistic results and quick solutions for hyperelastic continua, 2d triangular adaptive finite elements [40-42], 2d quadrilateral adaptive elements [35], 2d quadtree adaptive finite elements [43], 3d octree adaptive finite elements [44], and 3d tetrahedral adaptive finite elements [40,45] were used.

In this study, large deformations of a hyperelastic medium were calculated with three-dimensional hexahedral adaptive finite elements. A program was written in the MATLAB

environment using the total Lagrangian formulation. The results were examined by comparing them with Abaqus [46] software.

## 2. Theory and Formulation

### 2.1 Kinematics and Constitutive Theory

We consider the continuum shown in Fig. 1 to study the nonlinear motion of a nearly incompressible hyperelastic body. A continuous medium is shown that moves from the reference configuration, that is, the undeformed state, to the spatial configuration, that is, the deformed state, due to the forces and/or displacements acting on it. In subsequent calculations, scalar quantities are expressed in italics, and vector and tensor quantities are expressed in bold letters. Additionally, the elements of any vector or tensor are shown with index notation. Capital letters will be used in square brackets for matrices representing the elements of tensor quantities.

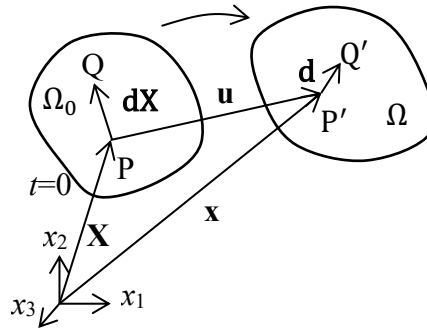


Fig. 1. Reference ( $\Omega_0$ ) and spatial configuration ( $\Omega$ ) of the continuous medium

The deformation gradient tensor is important for calculations involving large deformations in continuum mechanics. As seen in Eq. (1), the deformation gradient tensor  $\mathbf{F}$  is the tensor that transforms an infinitesimal  $d\mathbf{X}$  vector defined in the reference configuration into the  $d\mathbf{x}$  vector in the spatial configuration. It is defined as the derivative of the spatial position vector with respect to the reference position vector.

$$d\mathbf{x} = \mathbf{F}d\mathbf{X} \quad \text{veya} \quad F_{ij} = \frac{\partial x_i}{\partial X_j} \quad (1)$$

The strain energy function expressed in unit volume is used in the stress calculation for a hyperelastic continuum. For an isotropic medium, this quantity is expressed with the help of principal invariants in most cases. The principal invariants to be used here are the principal invariants of the Right Cauchy - Green deformation tensor  $\mathbf{C}$  given by Eq. (2).

$$\mathbf{C} = \mathbf{F}^T \mathbf{F} \quad (2)$$

The principal invariants of the right Cauchy - Green deformation tensor are written in terms of the eigenvalues of this tensor, as follows.

$$I_1 = \text{tr}(\mathbf{C}) = \lambda_1^2 + \lambda_2^2 + \lambda_3^2, \quad I_2 = \frac{1}{2} [(\text{tr}\mathbf{C})^2 - \text{tr}(\mathbf{C}^2)] = \lambda_1^2 \lambda_2^2 + \lambda_2^2 \lambda_3^2 + \lambda_3^2 \lambda_1^2, \quad I_3 = \det(\mathbf{C}) = \lambda_1^2 \lambda_2^2 \lambda_3^2 \quad (3)$$

Here,  $\lambda_1^2$ ,  $\lambda_2^2$  and  $\lambda_3^2$  represent the eigenvalues of the symmetric right Cauchy - Green deformation tensor,  $I_1$  and  $I_2$  represent the principal invariants related to distortion, and  $I_3$  represent the

principal invariant related to volumetric deformation. A general form of the strain energy function required for stress calculation is given in Eq. (4) [47].

$$W(I_1, I_2, I_3) = \sum_{m+n+k=1}^{\infty} C_{mnk} (I_1-3)^m (I_2-3)^n (I_3-1)^k \quad (4)$$

In this equation,  $C_{mnk}$  are the material coefficients. The strain energy function, which can be written by separating the distortional strain resulting from shear stresses and the volumetric strain resulting from normal stresses, is possible by using the following constants [47].

$$J_1 = I_1 I_3^{-1/3}, \quad J_2 = I_2 I_3^{2/3}, \quad J_3 = I_3^{1/2} \quad (5)$$

Here, the values  $J_1, J_2$  and  $J_3$  are reduced invariants.

Rubber-type materials used in engineering are called "nearly incompressible" because they can be compressed to a very low amount. The Mooney-Rivlin material model is often used when calculating the strain energy function of these hyperelastic materials because of its simple definition. Despite its difficulties representing the hardening of the material, it is a good model for large strains up to 100% strain [47]. There are four different types depending on the number of material constants used in the model. These are material models with 2, 3, 5 and 9 constants. For this model, the strain energy function is calculated with Eq. (6) using the reduced invariants given in Eq. (5). In this Equation,  $W_1$  refers to the distortion energy function and  $W_2$  refers to the energy function resulting from volumetric change.

$$W(J_1, J_2, J_3) = W_1(J_1, J_2) + W_2(J_3) = C_{10}(J_1-3) + C_{01}(J_2-3) + \frac{K}{2}(J_3-1)^2 \quad (6)$$

Here  $C_{10}, C_{01}$  are material constants and  $K$  is the bulk modulus. For a completely incompressible material, the bulk modulus should theoretically be infinite. For nearly incompressible medium, the solution using a large  $K$  value is referred to as the penalty method and  $K$  as the penalty parameter. In case of three-dimensional small unit strain, the value  $2(C_{10} + C_{01})$  corresponds to the shear modulus of the material, and the value  $6(C_{10} + C_{01})$  corresponds to the elasticity modulus of the material. Theoretically, for incompressible materials the Poisson's ratio should be 0,5, but for nearly incompressible behavior the Poisson's ratio is between 0,49 and 0,5.

The second Piola – Kirchhoff stress  $\mathbf{S}$  is obtained by the derivative of the strain energy function,  $W$ , with respect to the Lagrange strain tensor,  $\mathbf{E}$ , for the constitutive equations representing the relation between stress and strain, as follows,

$$\mathbf{S} = \frac{\partial W}{\partial \mathbf{E}} = \frac{\partial W_1}{\partial J_1} \frac{\partial J_1}{\partial \mathbf{E}} + \frac{\partial W_1}{\partial J_2} \frac{\partial J_2}{\partial \mathbf{E}} + \frac{\partial W_2}{\partial J_3} \frac{\partial J_3}{\partial \mathbf{E}} \quad (7)$$

The derivative of the second Piola – Kirchhoff stress with respect to the Lagrange strain tensor is equal to the fourth order constitutive tensor,  $\mathbf{D}$ .

$$\mathbf{D} = \frac{\partial \mathbf{S}}{\partial \mathbf{E}} \quad (8)$$

By calculating the tensor  $\mathbf{D}$  in terms of material constants, the relationship between stress and strain is established.

## 2.2 Nonlinear Finite Element Formulation

In the total Lagrangian formulation, the reference configuration of the continuum shown in Fig. 1 is used [48]. In addition, the frame of reference in this configuration is considered to be fixed. Independent variables are  $(\mathbf{X}, t)$  for position and time, and the displacement dependent variable is  $\mathbf{u}(\mathbf{X}, t)$ .

The "approximate displacement function" is expressed in terms of the shape functions written in the reference position and the displacements at the nodes as given in Eq. (9). Additionally, the displacement gradient and the Lagrange strain tensor are also written in terms of this "approximate displacement function" using spatial derivatives.

$$\begin{aligned} u_1 &= \sum_{j=1}^8 d_{1j}N_j = d_{11}N_1 + d_{12}N_2 + d_{13}N_3 + \dots + d_{18}N_8 \\ u_2 &= \sum_{j=1}^8 d_{2j}N_j = d_{21}N_1 + d_{22}N_2 + d_{23}N_3 + \dots + d_{28}N_8 \\ u_3 &= \sum_{j=1}^8 d_{3j}N_j = d_{31}N_1 + d_{32}N_2 + d_{33}N_3 + \dots + d_{38}N_8 \end{aligned} \quad (9)$$

According to the principle of minimum potential energy, the potential energy of the elastic system is equal to the difference between the stored strain energy  $\Pi_{int}$  in the system and the work done by external forces  $\Pi_{ext}$ . For an approximate solution in nonlinear finite element analysis, an iterative solution is made based on the principle of approximating this difference to the smallest value.

The strain energy stored in the system is calculated by integrating the strain energy density over the undeformed entire volume. The work done by the forces is calculated by the integral of the product of the body forces with the displacement of the nodes over the entire volume and the integral of the displacement of the nodes at the boundaries of the continuum multiplied by the external forces on the boundaries. Potential energy of the system can be written as follows.

$$\Pi = \Pi_{ext} - \Pi_{int} = \iiint_{\Omega_0} W(\mathbf{E})d\Omega - \iiint_{\Omega_0} \mathbf{u}^T \mathbf{f}_b d\Omega - \iint_{\tau_0} \mathbf{u}^T \mathbf{t} d\tau \quad (10)$$

If the displacement field  $\mathbf{u}$  is perturbed by  $\bar{\mathbf{u}}$  in an arbitrary direction and magnitude, equating the variation of potential energy  $\bar{\Pi}$  to zero yields the following variational equation.

$$\bar{\Pi} = \iiint_{\Omega_0} \frac{\partial W(\mathbf{E})}{\partial \mathbf{E}} : \bar{\mathbf{E}} d\Omega - \iiint_{\Omega_0} \bar{\mathbf{u}}^T \mathbf{f}_b d\Omega - \iint_{\tau_0} \bar{\mathbf{u}}^T \mathbf{t} d\tau = 0 \quad (11)$$

The displacement-strain transformation matrix  $[\mathbf{B}]$  relates nodal displacements to strain. In linear analysis, it only includes spatial derivatives of shape functions. It also includes the deformation gradient tensor for the nonlinear analysis. While it is constant in linear analysis, in nonlinear analysis it changes with respect to displacement because of the deformation gradient tensor.

Linear displacement-strain transformation matrix  $[\mathbf{B}_L]$ ,

$$[\mathbf{B}_L]=\begin{bmatrix} N_{1,1} & 0 & 0 & N_{2,1} & \dots & 0 & 0 \\ N_{1,2} & 0 & 0 & N_{2,2} & \dots & 0 & 0 \\ N_{1,3} & 0 & 0 & N_{2,3} & \dots & 0 & 0 \\ 0 & N_{1,1} & 0 & 0 & \dots & N_{8,1} & 0 \\ 0 & N_{1,2} & 0 & 0 & \dots & N_{8,2} & 0 \\ 0 & N_{1,3} & 0 & 0 & \dots & N_{8,3} & 0 \\ 0 & 0 & N_{1,1} & 0 & \dots & 0 & N_{8,1} \\ 0 & 0 & N_{1,2} & 0 & \dots & 0 & N_{8,2} \\ 0 & 0 & N_{1,3} & 0 & \dots & 0 & N_{8,3} \end{bmatrix} \quad (12)$$

and  $[\mathbf{B}_N]$  transformation matrix for nonlinear analysis is given by the following equation [47].

$$[\mathbf{B}_N]=\begin{bmatrix} F_{11}N_{1,1} & F_{21}N_{1,1} & F_{31}N_{1,1} & \dots & F_{31}N_{8,1} \\ F_{12}N_{1,2} & F_{22}N_{1,2} & F_{32}N_{1,2} & \dots & F_{32}N_{8,2} \\ F_{13}N_{1,3} & F_{23}N_{1,3} & F_{33}N_{1,3} & \dots & F_{33}N_{8,3} \\ F_{12}N_{1,1}+F_{11}N_{1,2} & F_{22}N_{1,1}+F_{21}N_{1,2} & F_{32}N_{1,1}+F_{31}N_{1,2} & \dots & F_{32}N_{8,1}+F_{31}N_{8,2} \\ F_{13}N_{1,2}+F_{12}N_{1,3} & F_{23}N_{1,2}+F_{22}N_{1,3} & F_{33}N_{1,2}+F_{32}N_{1,3} & \dots & F_{33}N_{8,2}+F_{32}N_{8,3} \\ F_{13}N_{1,1}+F_{11}N_{1,3} & F_{23}N_{1,1}+F_{21}N_{1,3} & F_{33}N_{1,1}+F_{31}N_{3,1} & \dots & F_{33}N_{8,1}+F_{31}N_{8,3} \end{bmatrix} \quad (13)$$

Here,  $N_I$  denotes the shape function and  $N_{Ij}$  denotes the derivative of the shape function with respect to position, and  $F_{ij}$  denotes the corresponding element of the deformation gradient.

Due to the nonlinearity in the displacement-strain relationship, there is no easy direct solution to the variational equations. It is possible to obtain the solution by the iterative Newton-Raphson method in combination with a series of successive linearizations.

Since internal forces are a nonlinear function of the deformation, the resulting force-displacement equation will need to be solved iteratively. A general nonlinear equation can be solved by the Newton-Raphson method along with a series of linearization operations. An iterative method such as the Newton-Raphson method requires the use of a tangent stiffness matrix. In the total Lagrangian formulation, the tangent stiffness matrix corresponds to the discretization of the linearized energy form. The 9x9 size  $[\Sigma]$  matrix, which will be used to obtain the linear part of the tangent stiffness matrix, is obtained with Eq. (14).

$$\bar{\mathbf{S}}=\begin{bmatrix} S_{11} & S_{12} & S_{13} \\ S_{21} & S_{22} & S_{23} \\ S_{31} & S_{32} & S_{33} \end{bmatrix}, \quad \bar{\mathbf{0}}=\begin{bmatrix} 0 & 0 & 0 \\ 0 & 0 & 0 \\ 0 & 0 & 0 \end{bmatrix}, \quad [\Sigma]=\begin{bmatrix} \bar{\mathbf{S}} & \bar{\mathbf{0}} & \bar{\mathbf{0}} \\ \bar{\mathbf{0}} & \bar{\mathbf{S}} & \bar{\mathbf{0}} \\ \bar{\mathbf{0}} & \bar{\mathbf{0}} & \bar{\mathbf{S}} \end{bmatrix} \quad (14)$$

Here  $\mathbf{S}$  is the second Piola-Krichhoff stress tensor. Tangent stiffness matrix  $[\mathbf{K}_T]$ , can be written by adding linear and non-linear parts as,

$$[\mathbf{K}_T]=\iiint_{\Omega_0}([\mathbf{B}_N]^T[\mathbf{D}][\mathbf{B}_N]+[\mathbf{B}_L]^T[\Sigma][\mathbf{B}_L])d\Omega \quad (15)$$

Generally, the integral in above equation is obtained by Gauss quadrature. 2x2x2 integration points were used for the hexahedral element.

Internal forces  $\mathbf{f}^{int}$  are obtained by the following discrete version of the energy form [47].

$$a(\mathbf{u}, \bar{\mathbf{u}}) = \iiint_{\Omega} \mathbf{S} : \bar{\mathbf{E}} \, d\Omega = \{\bar{\mathbf{d}}\}^T \iiint_{\Omega} [\mathbf{B}_N]^T \{\mathbf{S}\} \, d\Omega \equiv \{\bar{\mathbf{d}}\}^T \{\mathbf{f}^{int}\} \quad (16)$$

Using the minimum potential energy principle, the incremental finite element matrix equation is written as follows [47].

$$\{\bar{\mathbf{d}}\}^T [\mathbf{K}_T] \{\Delta \mathbf{d}\} = \{\bar{\mathbf{d}}\}^T \{\mathbf{f}^{ext} - \mathbf{f}^{int}\} \quad (17)$$

Here,  $\bar{\mathbf{d}}$  refers to the variation of nodal displacements,  $\Delta \mathbf{d}$  refers to the displacement increment,  $\mathbf{f}^{ext}$  refers to external forces,  $\mathbf{f}^{int}$  refers to internal forces. By making an initial assumption for node displacements, the increment in displacements,  $\Delta \mathbf{d}$ , is calculated from the solution of this system of equations and added to the existing node displacements to obtain the new displacement value of the nodes. Thus, one iteration is completed. Iterations continue until the difference between the external forces and internal forces on the right side of the equation approaches zero within a certain tolerance value.

### 2.3 Adaptive finite element mesh

Refinement of the finite element mesh is often done by the engineer performing the analysis. In the adaptive finite element mesh, refinement is done automatically according to a criterion determined independently of the person. The adaptive finite element mesh can be made in four different ways [49]. With the h-adaptive distribution, the size of the elements is changed; with the p-adaptive distribution, the degree of the element is changed; with the r-adaptive distribution, smaller finite elements are created in the targeted region by moving the mesh, provided that the degree and number of the elements are kept constant. The hp-adaptive distribution uses h- and p-methods together [49,50].

In this study, the h-adaptive method was used with hexahedral finite elements. In order to create the adaptive mesh, the minimum/maximum error indicator was used. The effective stress is the parameter of the minimum/maximum error indicator. In the minimum/maximum error distribution, the average parameter value of the finite elements is first found. The effective stress of all finite elements are compared with this value. If the element's effective stress is more or less than the average at a default value, the element is decided to be divided for the adaptive distribution.

The most commonly used method for mesh refinement is to divide an element into smaller elements. After this division process, the nodes formed in the finite element mesh should be connected to the nodes of another element, and the element edges or surfaces should not be formed in a way that cuts the edges and surfaces of other elements. The element types that can be used for division to achieve this are shown in Fig. 2. Here, an element that has not been divided will be named as a 0-element, and the divided element will be named according to the number of elements formed in it. The elements connecting the divided element to the mesh will be referred to as transition elements.

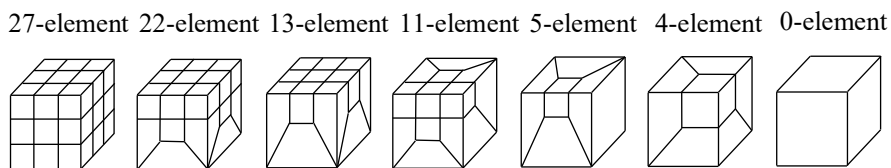


Fig. 2. Types of elements used in the refinement

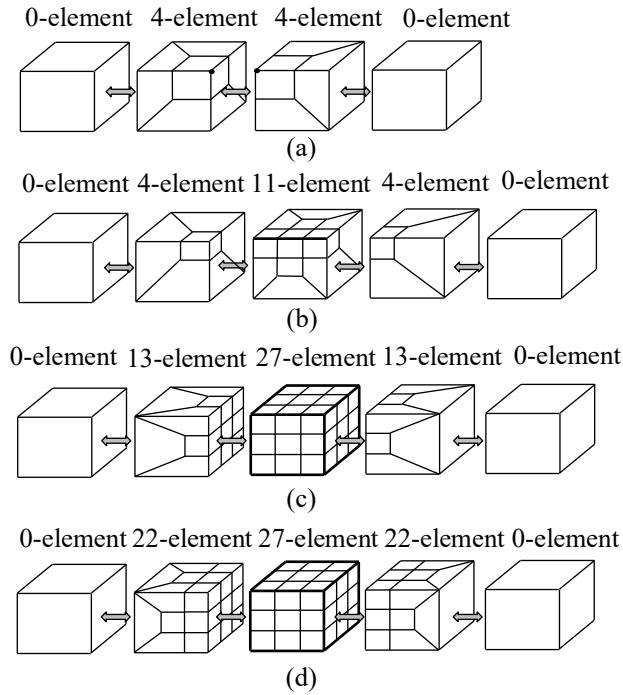


Fig. 3. Refinement strategies a) at a point, b) at an edge, c) and d) at an element

In the refinement, a new finite element mesh can be created using a node, element edge, and element surface or the element itself. If the refinement is decided to be done at a node as shown in Fig. 3a, the element is divided using a 4-element with the transition elements to connect the mesh. Fig. 4 shows a mesh refinement using a node of the mesh. If it is decided to refine the mesh by dividing the whole element, 27-element can be used with the transition elements as shown in Fig. 3c and 3d. The element types that can be connected to the divided element are expressed in Table 1. Additionally, new elements formed in a divided element are shown in Fig. 5.

Table 1. Elements that can be connected to a divided element

Divided element	Transition element
<b>27</b>	27, 22, 13
<b>22</b>	27, 22, 13, 11, 0
<b>13</b>	27, 22, 13, 5, 0
<b>11</b>	22, 11, 4, 0
<b>5</b>	13, 5, 0
<b>4</b>	11, 4, 0

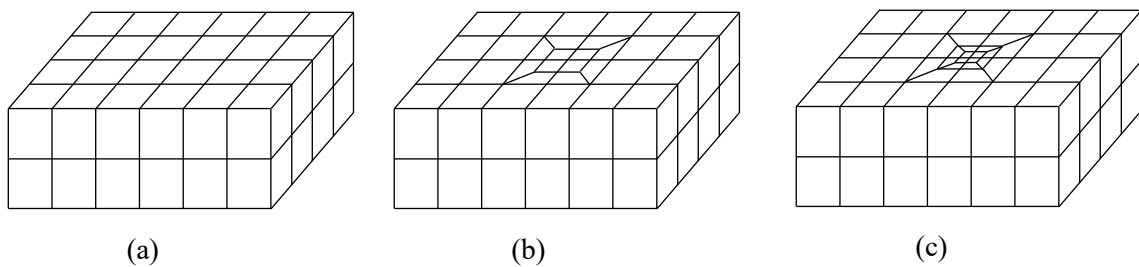


Fig. 4. Refinement of hexahedral mesh at a point on surface, a) initial element mesh, b) first refinement, c) second refinement



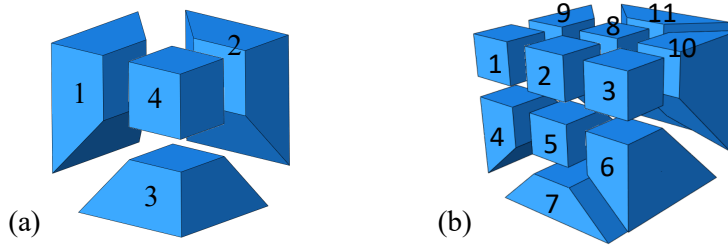


Fig. 5. Elements formed in a divided element for a) 4-element, b) 11-element

### 3. Analysis

Three specific examples were analyzed: the cubic block loaded with a single point loading, the rectangular block with shear loading, and the rectangular block containing a circular hole under uniform tension loading. Analyses were made by writing a code in MATLAB. In order to perform adaptive finite element analysis, an initial finite element analysis is made using an initial mesh. Then the mesh refinement is done using the stresses obtained. The final results are obtained by finite element analysis using the refined mesh.

In addition, the results were compared with the results obtained from ABAQUS finite element software, which is frequently used in the literature.

#### 3.1. Material properties

In the analyses, material constants  $C_{10}$  and  $C_{01}$  for the Mooney-Rivlin material model were taken as 0,552 MPa and 0,138 MPa, respectively. Within the small strain range, the shear modulus,  $G$ , of the material is equal to  $2(C_{10}+C_{01})$ , and it can be calculated as 1,38 MPa and the elasticity modulus,  $E$ , can be calculated as 4,14 MPa. Poisson's ratio can be calculated by the following equation.

$$\nu = \frac{\frac{3K}{2G} - 1}{\frac{3K}{G} + 1} \quad (18)$$

The bulk modulus is taken as 1000 MPa. The Poisson's ratio values calculated for different bulk moduli are given in Table 2. In the penalty method, a high  $K$  value causes an instability called "volumetric locking". A small change in displacement value leads to a large change in pressure due to the large  $K$  value. For this reason, the finite element exhibits a more rigid behavior and changes shape less. For nearly incompressible materials, it will be sufficient to use a  $K$  value that produces a Poisson's ratio close to 0.5.

Table 2. Poisson's ratio corresponding to certain bulk modulus values for  $C_{10} = 0,552$  and  $C_{01}=0,138$

<b>K (MPa)</b>	<b><math>\nu</math></b>
<b>1</b>	0,0274
<b>3</b>	0,3006
<b>5</b>	0,3736
<b>10</b>	0,4340
<b>100</b>	0,4931
<b>1000</b>	0,4993
<b>10000</b>	0,4999

### 3.2. Single point loading on a cubic block

The cubic block has a side length of 100 mm. Displacements of the bottom surface points are constrained as shown in Fig. 6a. Single point pressure loading was applied on mid point of the upper face of the block. Analyzes were made using adaptive mesh refinement. Initial mesh of the adaptive refinement has 216 uniformly distributed hexahedral elements as shown in Fig. 7a. Normal stress,  $\sigma_{22}$ , in the direction of the point load was used as the effective stress parameter for adaptive mesh refinement criterion. Two successive adaptive analyzes were made. Finite element meshes after two adaptive refinements are shown in Fig. 7b and 7c.

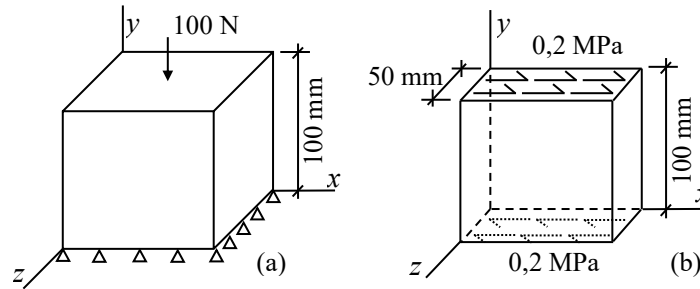


Fig. 6. a) Single point loading and b) shear loading applied on rectangular block

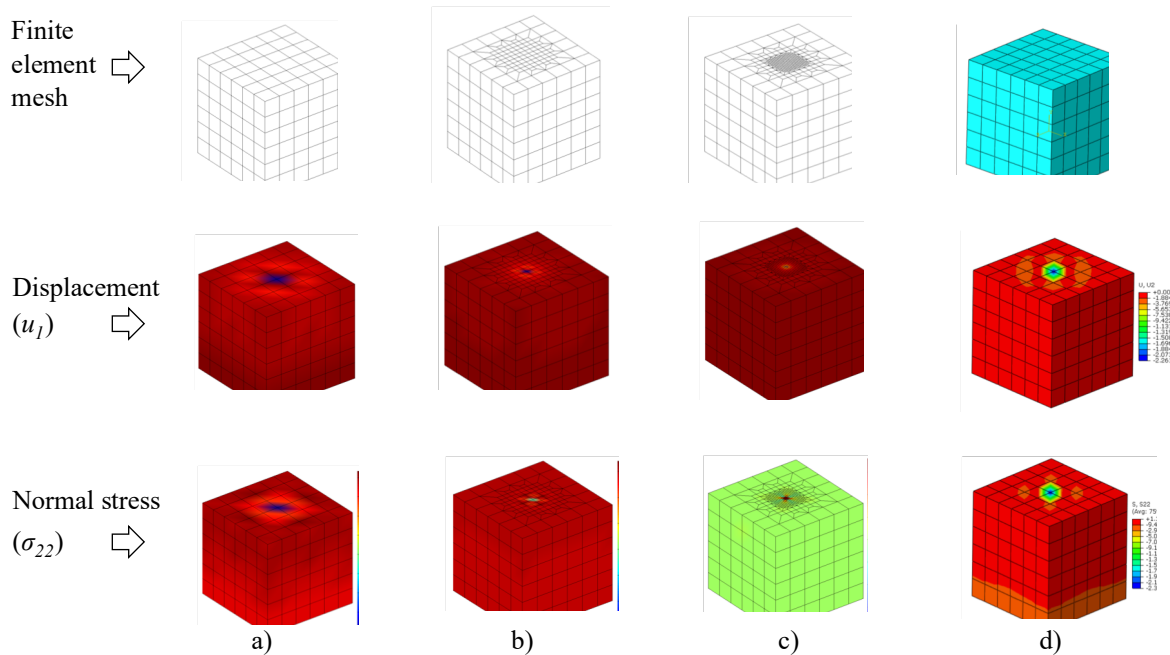


Fig. 7. a) initial mesh, b) first adaptive mesh refinement, c) second adaptive mesh refinement

The maximum displacement in  $y$ -direction,  $u_{2_{max}}$ , and maximum normal stress in  $y$ -direction,  $\sigma_{22_{max}}$ , are shown in Table 3. After the second adaptive analysis, the number of elements increases to 3108 elements, and the minimum element edge length decreases to 1,85, that is 11% of the minimum element edge length of the initial mesh.

The maximum displacement in the  $y$ -direction occurs at the point of application of the force. Its value varies between 2,18 mm and 7,63 mm as the number of elements increases for adaptive finite element analysis. The maximum normal stress occurs at the point of application of the

force. It varies between 0,164 MPa and 0,811 MPa as the number of elements increases for adaptive finite element analysis.

Table 3. Maximum  $u_2$  displacement and maximum  $\sigma_{22}$  stress for adaptive mesh refinement

Analysis name	Number of elements	Minimum element edge length (mm)	$u_{2,max}$ (mm)	$\sigma_{22,max}$ (MPa)
Initial mesh analysis	216	16,7	2,18	0,164
First adaptive analysis	1016	5,55	6,17	0,791
Second adaptive analysis	3108	1,85	8,05	0,811

In addition, analyzes were also made using uniform mesh refinement where all the elements in the mesh were divided. Maximum displacement in  $y$ -direction and corresponding maximum normal stress obtained after four consecutive analyzes, are shown in Table 4. After the 4<sup>th</sup> uniform mesh refinement, the number of elements increases to 2744 elements, and the minimum element edge length decreases to 7,14, that is 43% of the minimum element edge length of the initial mesh.

Table 4. Maximum  $u_2$  displacement and maximum  $\sigma_{22}$  stress for uniform mesh refinement

Analysis #	Number of elements	Minimum element edge length (mm)	$u_{2,max}$ (mm)	$u_{2,max}$ (mm) (Abaqus)	Difference (%)	$\sigma_{22,max}$ (MPa)	$\sigma_{22,max}$ (MPa) (Abaqus)	Difference (%)
1	216	16,7	2,18	2,26	3,54	0,164	0,234	29,91
2	512	12,5	2,86	2,96	3,38	0,265	0,373	28,95
3	1000	10	3,52	3,6	2,22	0,364	0,497	26,76
4	2744	7,14	4,76	4,89	2,66	0,538	0,892	39,69

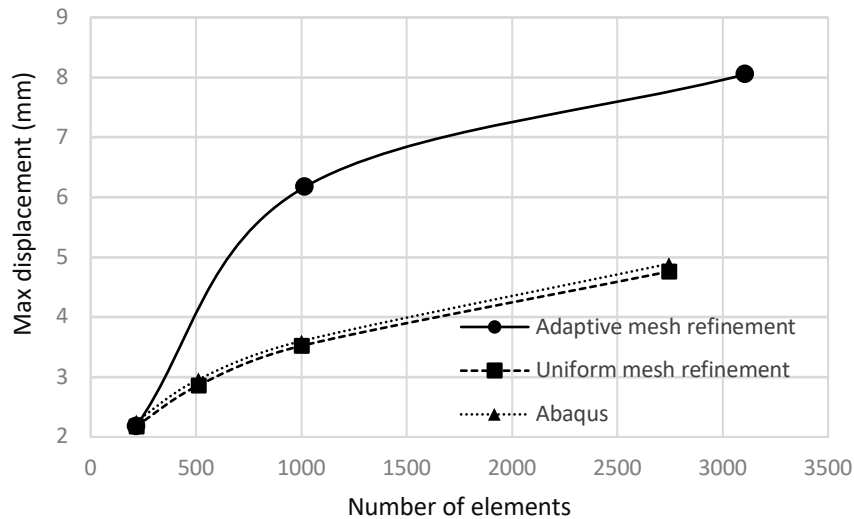


Fig. 8. Variation of maximum displacement  $u_{2,max}$  with the number of elements

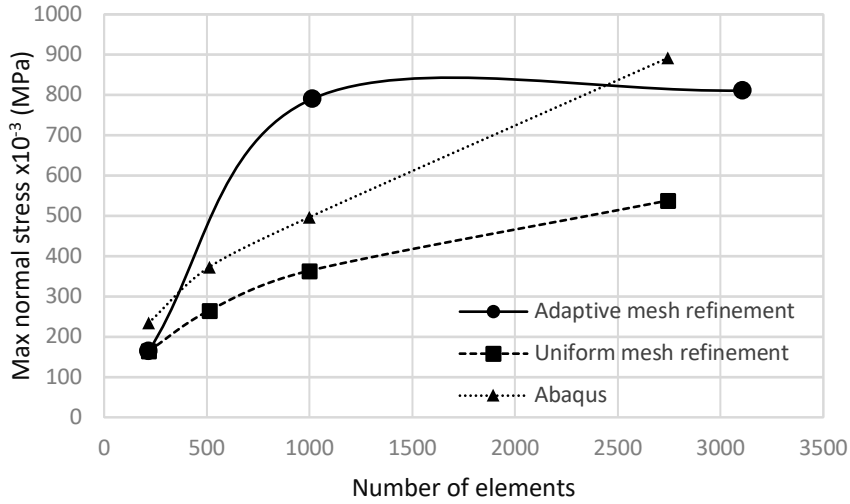


Fig. 9. Variation of maximum normal stress  $\sigma_{22_{max}}$  with number of elements

In uniform mesh refinement, maximum displacement in the  $y$ -direction varies between 2,18 mm and 4,76 mm. The % difference between the results of uniform mesh refinement and Abaqus decreases as the number of elements increases.

Fig. 8 and Fig. 9 show the variation of maximum displacement,  $u_{2_{max}}$ , and variation of the maximum normal stress,  $\sigma_{22_{max}}$ , with the number of elements. These graphs represent convergence when adaptive mesh refinement was used.

### 3.3. Shear loading from the top surface on a rectangular block

The rectangular block, shown in Fig. 6b, is loaded at the bottom and top surface with a tangential surface traction of 0,2 MPa. Analyzes were made using two consecutive adaptive mesh refinements. Shear stress,  $\sigma_{12}$ , was used as the effective stress parameter for adaptive mesh refinement criterion. The number of elements created is given in Table 5. Maximum displacement in the  $x$ -direction,  $u_{1_{max}}$ , was calculated near the top and bottom edge of the problem geometry in the force direction. The maximum value of shear stress,  $\sigma_{12_{max}}$ , was obtained in the mid region of the problem geometry. The variation of maximum displacement in the  $x$ -direction,  $u_{1_{max}}$ , and variation of maximum shear stresses,  $\sigma_{12_{max}}$ , with the number of elements are shown in Fig. 10 and Fig. 11, respectively. Adaptive analysis converged after the first adaptive mesh refinement.

Table 5. Maximum  $u_1$  displacement and maximum shear  $\sigma_{12}$  stress for adaptive mesh refinement

Analysis name	Number of elements	Minimum element edge length (mm)	$u_{1_{max}}$ (mm)	$\sigma_{12_{max}}$ (MPa)
Initial mesh analysis	108	16,7	9,73	0,265
First adaptive analysis	1542	5,55	10,12	0,277
Second adaptive analysis	10920	1,85	10,14	0,279

Analyzes were also performed using five uniform meshes by increasing the number of elements, as shown in Table 6. The problem was also analyzed using the Abaqus software with identical mesh distributions. Code written in MATLAB and Abaqus software yields similar results for

uniform mesh refinement. The maximum displacement value,  $u_{1_{max}}$ , and maximum shear stress,  $\sigma_{12_{max}}$ , for uniform mesh refinement apparently converged as the number of elements increased.

Table 6. Maximum  $u_1$  displacement and maximum  $\sigma_{12}$  stress values for various uniform mesh refinements

Analysis #	Number of elements	Minimum element edge length (mm)	$u_{1_{max}}$ (m)	$u_{1_{max}}$ (mm) (Abaqus)	Difference (%)	$\sigma_{12_{max}}$ (MPa)	$\sigma_{12_{max}}$ (MPa) (Abaqus)	Difference (%)
1	108	16,7	9,73	10,31	5,63	0,265	0,283	6,36
2	256	12,5	10,18	10,39	2,02	0,279	0,289	3,46
3	500	10	10,31	10,47	1,53	0,286	0,292	2,05
4	864	8,33	10,40	10,50	0,95	0,290	0,293	1,02
5	4000	5	10,52	10,60	0,75	0,294	0,297	1,01

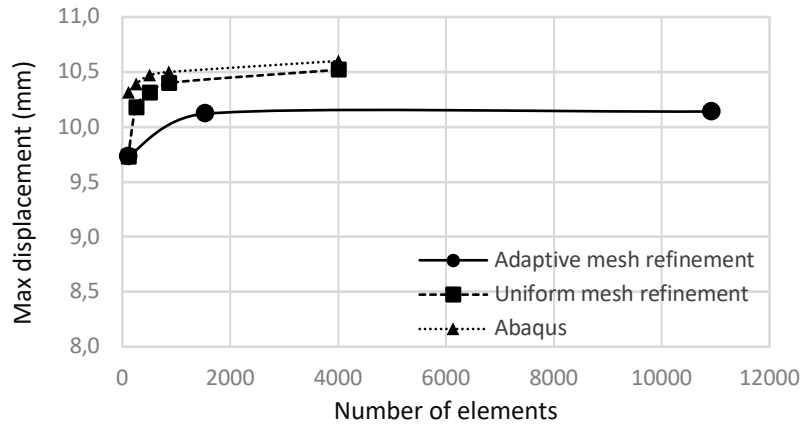


Fig. 10. Variation of maximum displacement  $u_{1_{max}}$  with number of elements

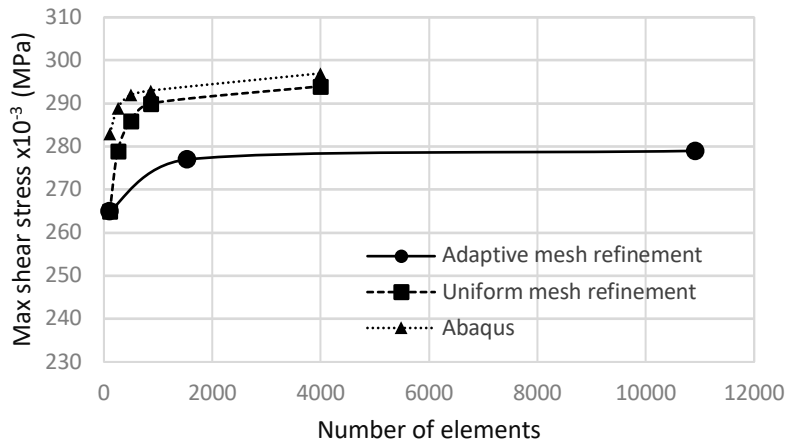


Fig. 11. Variation of maximum shear stress  $\sigma_{12_{max}}$  with number of elements

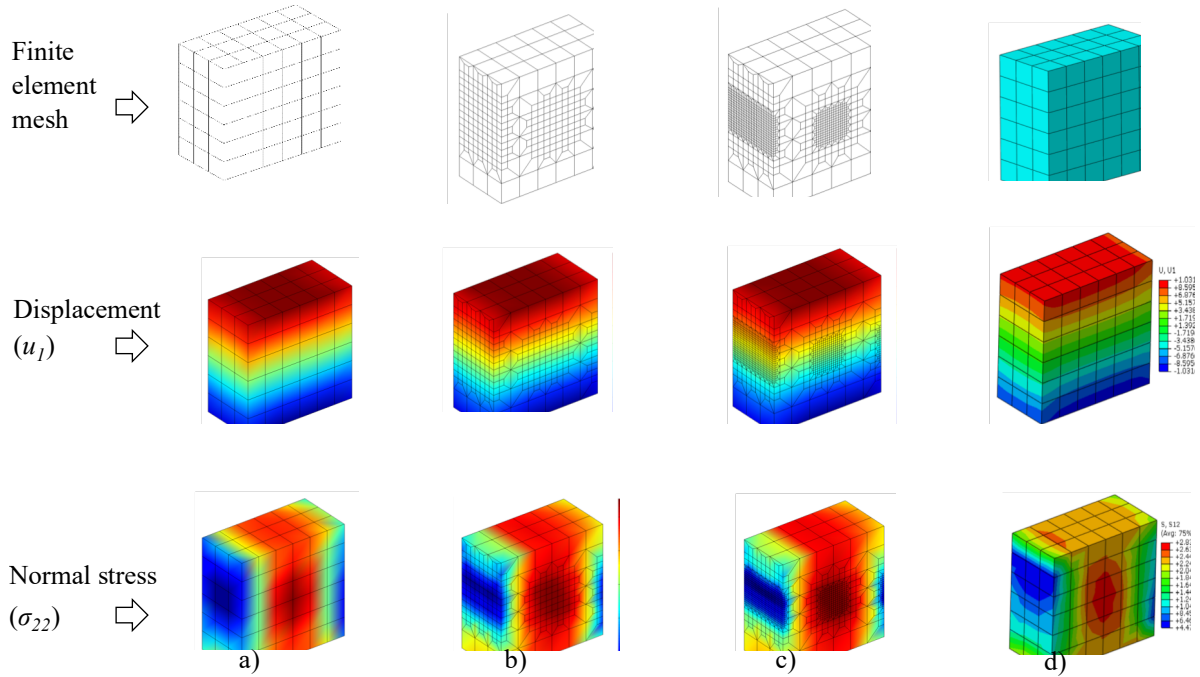


Fig. 12. Variation of displacement ( $u_1$ ) and shear stress ( $\sigma_{12}$ ) obtained from a) initial mesh, b) first adaptive mesh, c) second adaptive mesh, d) Abaqus

### 3.4. Rectangular block with circular hole

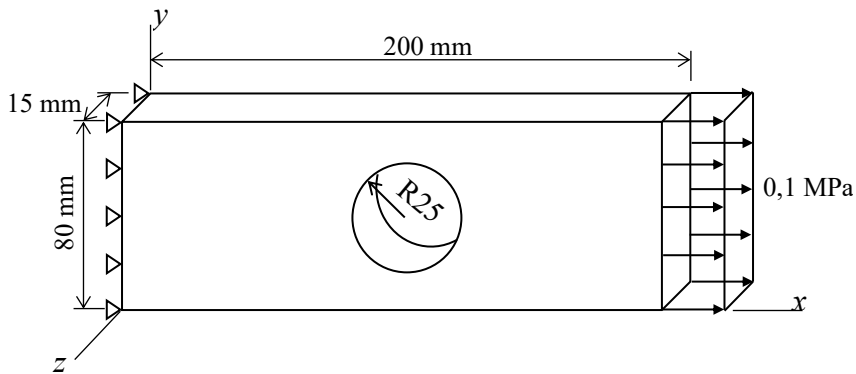


Fig. 13. Problem geometry, boundary conditions and applied force

Among the problems involving geometric discontinuities, the most frequently used problem geometry is a continuous medium containing a circular hole. Dimension of such a geometry is given in Fig. 13. The nodes on left end of the rectangular block is restrained not to move along the  $x$ -direction and a distributed load is applied on the right end as the boundary conditions.

After the initial finite element mesh was created using 600 elements, two consecutive adaptive analyzes were carried. Normal stress,  $\sigma_{11}$ , in the direction of the tension load was used as the effective stress parameter for adaptive mesh refinement criterion. In Table 7, the maximum values of displacement in the  $x$ -direction and maximum normal stress obtained from these adaptive analyzes are presented. Also, the variation of displacements and shear stresses are shown in Fig. 14.

Table 7. Maximum  $u_I$  displacement and maximum  $\sigma_{II}$  stress obtained from adaptive mesh refinement

Analysis name	Number of elements	Smallest element edge length (mm)	$u_{I_{max}}$ (mm)	$\sigma_{II_{max}}$ (MPa)
Initial mesh analysis	600	6,54	7,61	0,435
First adaptive analysis	2230	2,18	7,81	0,509
Second adaptive analysis	11770	0,73	7,81	0,594

Maximum normal stresses  $\sigma_{II_{max}}$  were observed at the lower and upper midpoints of the circular hole. Maximum displacements  $u_{I_{max}}$  were observed at the midpoint of the upper and lower edges of the surface to which the load is applied.

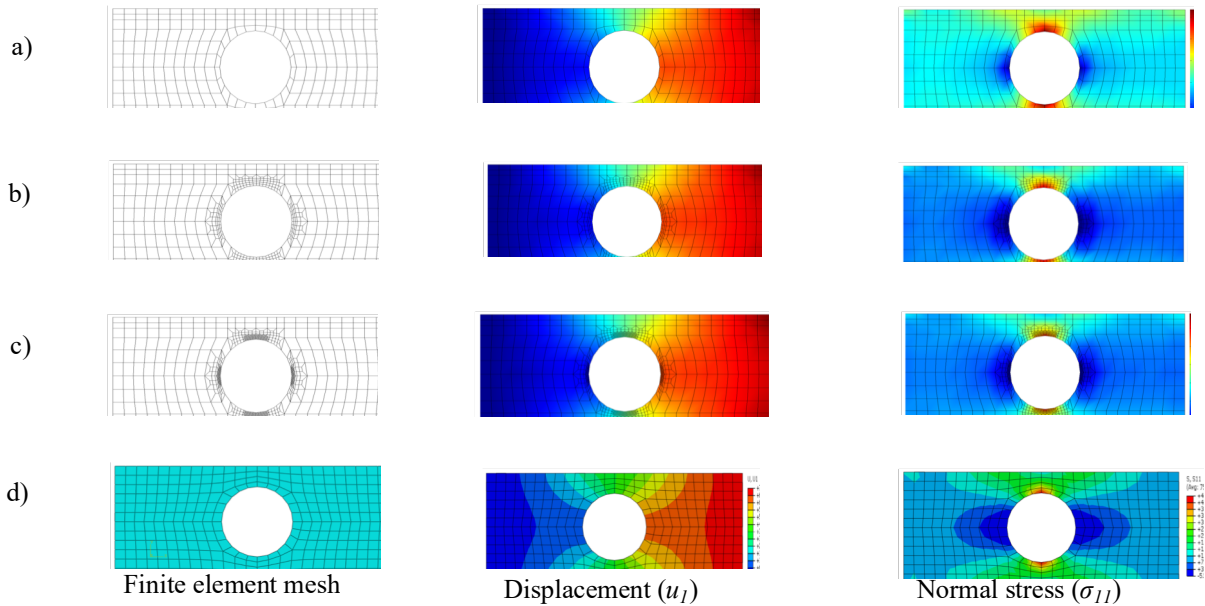


Fig. 14. Variation of displacement ( $u_I$ ) and normal stress ( $\sigma_{II}$ ) obtained from a) initial mesh, b) first adaptive mesh, c) second adaptive mesh, d) Abaqus

Analysis also was carried out for five separate uniform finite element meshes. The results for the maximum displacement,  $u_{I_{max}}$ , and maximum normal stress,  $\sigma_{II_{max}}$ , obtained using these meshes are shown in Table 8 in comparison with the results of Abaqus.

Fig. 14 and Fig. 15 show that the displacements were converged for the adaptive mesh analysis, and the normal stresses almost converged after second refinement. It has been also observed that the code written in MATLAB and Abaqus yield convergent solutions for the displacements and normal stresses in uniform distributions.

Table 8. Maximum  $u_I$  displacement and maximum  $\sigma_{II}$  stress

Analys #	Number of elements	Smallest element edge length (mm)	$u_{I_{max}}$ (m)	$u_{I_{max}}$ (mm) (Abaqus)	Difference (%)	$\sigma_{II_{max}}$ (MPa)	$\sigma_{II_{max}}$ (MPa) (Abaqus)	Difference (%)
1	600	6,54	7,61	7,5	-1,47	0,435	0,480	9,38
2	1332	4,91	7,63	7,57	-0,79	0,442	0,487	9,24
3	1932	3,93	7,65	7,61	-0,53	0,450	0,491	8,35
4	3360	3,27	7,65	7,62	-0,39	0,464	0,497	6,64
5	4260	2,8	7,66	7,63	-0,39	0,465	0,499	6,81

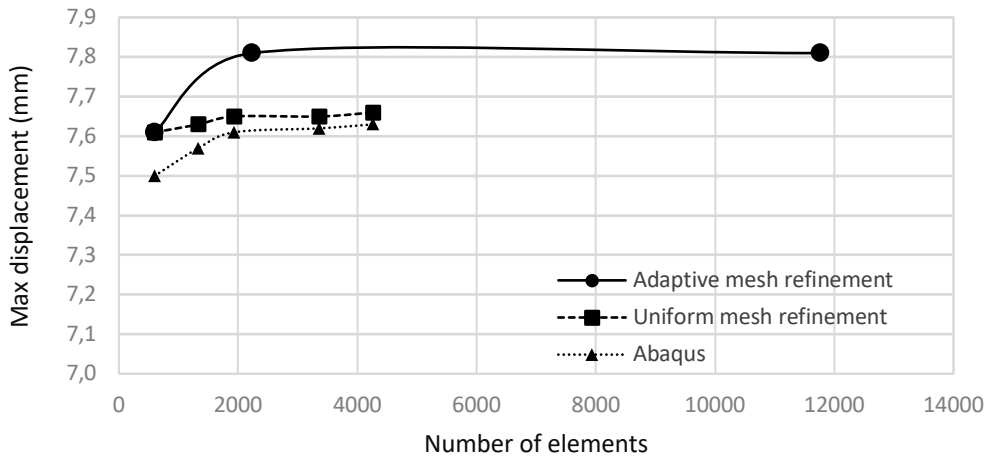


Fig.14. Variation of maximum displacement  $u_{I_{max}}$  with number of elements

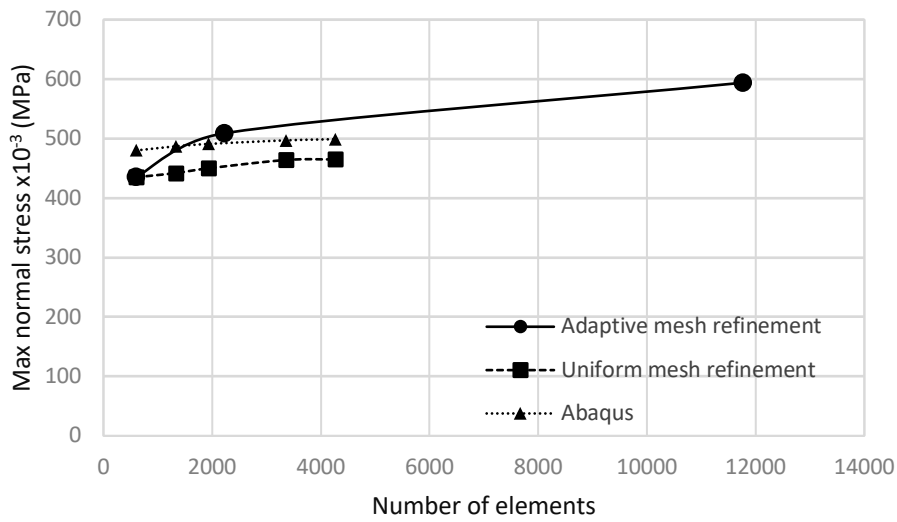


Fig.15. Variation of maximum normal stress  $\sigma_{II_{max}}$  with number of elements



#### 4. Conclusions

In this study, considering the large deformation of hyperelastic continuum, displacement and stress calculations were made using the Mooney-Rivlin material model and adaptive finite element analysis with hexahedral elements. Although there are sufficient studies on creating adaptive mesh using hexahedral elements, new studies are needed on its use for large deformation calculations with the finite element method. In this regard, a code has been written in the MATLAB environment. In order to check the reliability of the code, the test problems with the uniform mesh distributions were also solved with the Abaqus software. Comparisons show that the code written in MATLAB and Abaqus yields compatible results. Adaptive mesh refinement of hexahedral elements in the finite element analysis was performed using transition elements.

For the example of single point loading on a cubic block, the smallest element edge length decreased by approximately 90 percent in the adaptive finite element mesh, and the maximum displacement ( $u_2$ ) and maximum normal stress ( $\sigma_{22}$ ) values converged after the first adaptive solution. In the uniform mesh, the smallest element edge length decreased by approximately 60 percent. Maximum displacement ( $u_2$ ) and maximum normal stress ( $\sigma_{22}$ ) values converged faster than the adaptive finite element results. The maximum normal stress ( $\sigma_{22}$ ) value obtained from the adaptive solution is approximately 10 percent less than the Abaqus solution.

For the shear loading from the top and bottom surfaces, the smallest element edge length decreased by approximately 90 percent in the adaptive mesh. The maximum displacement ( $u_1$ ) and maximum shear stress ( $\sigma_{12}$ ) values converged after the first adaptive solution. In the uniform mesh, the smallest element edge length decreased by approximately 70 percent. The maximum displacement ( $u_1$ ) and maximum shear stress ( $\sigma_{12}$ ) values converged for both the adaptive mesh refinement and the uniform mesh. The adaptive solution maximum shear stress ( $\sigma_{12}$ ) value is approximately 6 percent less than the Abaqus.

For the rectangular block with a circular hole, the smallest element edge length around the circle decreased by approximately 90 percent in the adaptive mesh refinement. The maximum displacement ( $u_1$ ) values converged after the first adaptive solution. The smallest element edge length decreased by approximately 60 percent in the uniform mesh. The maximum displacement value converged to 7,8mm after the first adaptive refinement. The maximum normal stress ( $\sigma_{11}$ ) value almost converged for the uniform mesh. The difference between the results of the adaptive finite element solution and uniform mesh solution is approximately 16 percent for the maximum normal stress ( $\sigma_{11}$ ) value.

The displacements obtained from the finite element solutions are large; for example, the displacements were between 4% and 11% of the problem geometry.

In order to create a uniform mesh distribution with the smallest element size as in the adaptive mesh refinement, many more elements need to be used. In this case, the solution time increases. Thus, adaptive distribution provides an advantage by shortening the solution time.

It can be seen that the criterion used in adaptive mesh refinement effectively creates locally refined elements.

For local mesh refinements, the transition from large to small elements must be smooth. In the case of hexahedral elements, the use of transition elements causes the formation of sharp internal angle elements in the transition from the larger to the smaller elements. In this case, the element mesh is not smooth enough. Considering the effect of this situation on the results, a smoothing procedure can be recommended to improve the results.

More realistic simulations can be made for tearing/rupture due to large deformations of the hyperelastic continuum by using adaptive mesh refinement with hexahedral elements.

## References

- [1] Blacker, T., Automated conformal hexahedral meshing constraints, challenges and opportunities. *Engineering with Computers*, 17, 201-210, 2002.
- [2] Tadepalli, S.C., Erdemir, A. and Cavanagh, P.R., Comparison of hexahedral and tetrahedral elements in finite element analysis of the foot and footwear. *Journal of Biomechanics*, 44, 2337-2343, 2011.
- [3] Schneiders, R., A grid-based algorithm for the generation of hexahedral element meshes. *Engineering with Computers*, 12, 168-177, 1996.
- [4] Eppstein, E., Linear complexity hexahedral mesh generation. *Computational Geometry Theory and Applications*, 12, 3-16, 1999.
- [5] Baudouin, T.C., Remacle, J.F., Marchandise, E., Henrotte, F. and Geuzaine, C., A frontal approach to hex-dominant mesh generation. *Advanced Modeling and Simulation in Engineering Sciences*, 1-8, 2014.
- [6] Staten, M.L., Canann, S.A. and Owen, S.J., *BMSweep: Locating interior nodes during sweeping*. *Engineering with Computers*, 15, 212-218, 1999.
- [7] Lai, M., Benzley, S. and White, D., Automated hexahedral mesh generation by generalized multiple source to multiple target sweeping. *International Journal for Numerical Methods in Engineering*, 49, 261-275, 2000.
- [8] Owen, S.J. and Saigal, S., H-Morph: an indirect approach to advancing front hex meshing. *International Journal for Numerical Methods in Engineering*, 49, 289-312, 2000.
- [9] Li, T.S., McKeag, R.M. and Armstrong, C.G., Hexahedral meshing using midpoint subdivision and integer programming. *Computer Methods in Applied Mechanics and Engineering*, 124, 171-193, 1995.
- [10] Schneiders, R., Refining quadrilateral and hexahedral element meshes, *Proceedings of the Fifth International Conference on Numerical Grid Generation in Computational Field Simulations*, 679-688, 1996.
- [11] Harris, N.J., Benzley, S.E. and Owen, S.J., Conformal refinement of all-hexahedral element meshes based on multiple twist plane insertion, *Proceedings of the 13th International Meshing Roundtable (IMR)*, 157-168, 2004.
- [12] Parrish, M., Borden, M., Staten, M. and Benzley, S., A selective approach to conformal refinement of unstructured hexahedral finite element meshes, *Proceedings of the 16th International Meshing Roundtable (IMR)*, Seattle, USA, 14-17 Oct 2007.
- [13] Huang, L., Zhao, G., Wang, Z. and Zhang, X., Adaptive hexahedral mesh generation and regeneration using an improved grid-based method. *Advances in Engineering Software*, 102, 49-70, 2016.

- [14] Huang, L., Zhao, G., Ma, X. and Wang, Z., Incorporating improved refinement techniques for a grid-based geometrically-adaptive hexahedral mesh generation algorithm. *Advances in Engineering Software*, 64, 20-32, 2013.
- [15] Tchon, K.F., Khachan, M., Guibault, F. and Camarero, R., Three-dimensional anisotropic geometric metrics based on local domain curvature and thickness. *Computer-Aided Design*, 37, 173-187, 2005.
- [16] Zhang, Y. and Bajaj, C., Adaptive and quality quadrilateral/hexahedral meshing from volumetric data. *Computer Methods Applied Mechanics and Engineering*, 195, 942–960, 2006.
- [17] Fernandes, J.L.M. and Martins, P.A.F., All-hexahedral remeshing for the finite element analysis of metal forming processes. *Finite Elements in Analysis and Design*, 43, 666 – 679, 2007.
- [18] Zhao, G., Zhang, H. and Cheng, L., Geometry-adaptive generation algorithm and boundary match method for initial hexahedral element mesh. *Engineering with Computers*, 24, 321–339, 2008.
- [19] Sun, L., Zhao, G. and Ma, X., Adaptive generation and local refinement methods of three-dimensional hexahedral element mesh. *Finite Elements in Analysis and Design*, 50, 184–200, 2012.
- [20] Zhu, J. and Zienkiewicz, C., Super convergence recovery technique and a posteriori error estimators. *International Journal for Numerical Methods in Engineering*, 30, 1321-1339, 1990.
- [21] Devloo, P. R., A three-dimensional adaptive finite element strategy. *Computers and Structures*, 38, 121-130, 1991.
- [22] Zienkiewicz, O.C. and Zhu, J.Z., The superconvergent patch recover (SPR) and adaptive finite element refinement. *Computer Methods in Applied Mechanics and Engineering*, 101, 207-224, 1992.
- [23] Wada, Y. and Okuda, H., *Effective adaptation technique for hexahedral mesh. Concurrency and Computation: Practice And Experience*, 14, 451-463, 2002.
- [24] Park, C.,H. and Yang, D.Y., Adaptive refinement of all-hexahedral elements for three-dimensional metal forming analysis. *Finite Elements in Analysis and Design*, 43, 22–35, 2006.
- [25] Moshfegh, R., Li, X. and Nilsson, L., Gradient-based refinement indicators in adaptive finite element analysis with special reference to sheet metal forming. *Engineering Computations*, 17, 910-932, 2000.
- [26] Niekamp, R. and Stein, E., An object-oriented approach for parallel two- and three-dimensional adaptive finite element computations. *Computers and Structures*, 80, 317–328, 2002.
- [27] Swanson, S. R., Large deformation finite element calculations for slightly compressible hyperelastic materials. *Computers and Structures*, 21, 81-88, 1985.

- [28] Pengt, S. H. and Cbang, W. V., A compressible approach in finite element analysis of rubber-elastic materials. *Computers and Structures*, 62, 573-593, 1997.
- [29] Suchocki, C., Finite element implementation of slightly compressible and incompressible first invariant-based hyperelasticity: theory, coding, exemplary problems. *Journal of Theoretical and Applied Mechanics*, 55, 787-800, 2017.
- [30] Herrmann, L. R., Elasticity equations for incompressible and nearly incompressible materials by a variational theorem. *American Institute of Aeronautics and Astronautics (AIAA) Journal*, 3, 1896-1900, 1965.
- [31] Bonet, J. and Bhargava, P., A uniform deformation gradient hexahedron element with artificial hourglass control. *International Journal For Numerical Methods in Engineering*, 38, 2809-2828, 1995.
- [32] Neto, E. A. S., Peril D., Dutko M. and Owen D. R. J., Design of simple low order finite elements for large strain analysis of nearly incompressible solids. *International Journal of Solids and Structures*, 33, 3211-3296, 1996.
- [33] Pascon, J. P., Large deformation analysis of plane-stress hyperelastic problems via triangular membrane finite elements. *International Journal of Advanced Structural Engineering*, 11, 331-350, 2019.
- [34] Medri, G. and Strozzi, A., Mechanical analysis of elastomeric seals by numerical methods. *Industrial and Engineering Chemistry Product Research and Development*, 23, 596-600, 1984.
- [35] Kato, K., Lee, N.S. and Bathe K.J., Adaptive finite element analysis of large strain elastic response. *Computers and Structures*, 47, 829-855, 1993.
- [36] Chamberland, E., Fortin, A. and Fortin, M., Comparison of the performance of some finite element discretizations for large deformation elasticity problems. *Computers and Structures*, 88, 664-673, 2010.
- [37] O'Shea, D. J., Attard, M. M., Kellermann, D.C. and Sansour, C., Nonlinear finite element formulation based on invariant-free hyperelasticity for orthotropic materials. *International Journal of Solids and Structures*, 185, 191-201, 2000.
- [38] Nguyen, T. D., Huynh, T. T. H., Nguyen, N. T., Nguyen, H. T. M. and Truong, T. T., Finite element analysis for three-dimensional hyper-elastic problems. *Science and Technology Development Journal*, 24, 43-50, 2022.
- [39] Schönherr, J. A., Schneider, P. and Mittelstedt, C., Robust hybrid/mixed finite elements for rubber-like materials under. *Computational Mechanics*, 70, 101-122, 2022.
- [40] Onishi, Y. and Amaya, K., A locking-free selective smoothed finite element method using tetrahedral and triangular elements with adaptive mesh rezoning for large deformation problems. *International Journal for Numerical Methods in Engineering*, 99, 354-371, 2014.
- [41] Léger, S., Fortin, A., Tibirna, C. and Fortin, M., An updated Lagrangian method with error estimation and adaptive remeshing for very large deformation elasticity problems. *International Journal For Numerical Methods in Engineering*, 100, 1006-1030, 2014.

- [42] Ju, X., Mahnken, R., Xu, Y. and Liang, L., Goal-oriented error estimation and h-adaptive finite elements for hyperelastic micromorphic continua. *Computational Mechanics*, 69, 847-863, 2022.
- [43] Jansaria, C., Natarajana, S., Beexb, L. and Kannana, K., Goal-oriented error estimation and h-adaptive finite elements for hyperelastic micromorphic continua. *Computational Mechanics*, 69, 847–863, 2022.
- [44] Meyer, A., Error estimators and the adaptive finite element method on large strain deformation problems. *Mathematical Methods in the Applied Sciences*, 32, 2148-2159, 2009.
- [45] Léger, S. and Pepin, A., An updated Lagrangian method with error estimation and adaptive remeshing for very large deformation elasticity problems: The three-dimensional case. *Computer Methods Applied Mechanics and Engineering*, 309, 1–18, 2016.
- [46] Smith, M., *ABAQUS/Standard User's Manual*, Version 6.9, Dassault Systemes, Simulia Corp, 2009.
- [47] Kim, N.H., *Introduction to Nonlinear Finite Element Analysis*, Springer, 2015.
- [48] Shabana, A.A. and Niamathullah, S.K., Total Lagrangian Formulation For Large-Displacement Analysis Of The Triangular Finite Elements. *Computer Methods in Applied Mechanics And Engineering*, 72, 195-199, 1989.
- [49] Wriggers, P., *Nonlinear Finite Element Methods*, Springer, 2008.
- [50] Zienkiewicz, O.C., Zhu, J.Z. and Gong, N.G., Effective and Practical h–p Adaptive Analysis Procedure for the Finite Element Method, *International Journal for Numerical Methods in Engineering*, 28, 879-891, 1989.



## A Charging Station Planning Study to Prepare for the Utilization of Electric Vehicles on University Campuses: The Case of Ondokuz Mayıs University

Metin Mutlu AYDIN

Ondokuz Mayıs University, Faculty of Engineering, Department of Civil Engineering, Samsun, 55270, Türkiye

✉: [metinmutluaydin@gmail.com](mailto:metinmutluaydin@gmail.com) : 0000-0001-9470-716X

Received: 21.10.2023, Revised: 14.12.2023, Accepted: 17.12.2023

### Abstract

Electric vehicles (EVs) have gained significant interest as a cleaner and sustainable mode of transportation compared to fossil-fuel vehicles. Although its background goes beyond a century ago, the effects of global warming have increased the development and utilization of EVs. Similarly, serious investments are being made for the development and use of EVs for batteries and charging stations, and, R&D activities are being carried out in Türkiye. With the start of domestic e-Car utilization, it is expected that e-Cars will be used throughout Türkiye. Therefore, charging stations will be established to meet needs. For this scope, a design study has been conducted at Ondokuz Mayıs University Campus and the number of stations was determined to ensure the effective use of e-Cars at the campus. A field study was conducted on the current parking lots, their capacities, and average occupancy rates. Then, charging station recommendations were developed for each parking lot based on the distribution of EVs by correlating the parking lot capacities, occupancy rates, and distribution. With similar planning to be carried out on other university campuses, universities will be at the forefront of e-Car utilization and many studies can be conducted to solve the problems that will be identified.

**Keywords:** Electric cars, charging station, parking lot planning, vehicle utilization.

### 1. Introduction

Since their first appearance in the 18th century, vehicles have evolved into hundreds of different forms. According to available statistics, there are more than 1.5 billion wheeled vehicles in the world today, used in various sectors ranging from logistics, public transport and travel to the service sector [1]. As a result, vehicles have become very important in the global economy, both for saving time and for transporting people and goods. Although these vehicles save time and perform important services, they have a negative impact on the environment due to the harmful gases they emit as they have internal combustion engines [2,3].

in recent years due to the harmful gases emitted into the environment and the destruction of nature by humans [4,5]. According to the statistics of the US Environmental Protection Agency, 76% of the greenhouse gas emissions that cause global warming are CO<sub>2</sub> emissions and 29% of these CO<sub>2</sub> gas emissions are caused by the transport sector [1]. Due to this result and the fact that global warming is becoming more noticeable every day, global vehicle manufacturers have focused on developing vehicles that use green energy and have net-zero emissions instead of using vehicles that use fossil fuels [6,7].

In recent years, many fuel types have been developed and actively used in vehicles as an alternative to fossil fuels due to technological developments [8]. The most prominent of these are hydrogen-fuelled vehicles, plug-in hybrid vehicles and electric vehicles [9]. Hydrogen-fuelled vehicles (HFVs) move by burning hydrogen stored in cells, while electric vehicles (EVs) use electricity stored in batteries for energy. Although these two types are considered to be the



most environmentally friendly new generation of vehicle engines, electric vehicles are more popular and preferred in today's conditions [10]. Looking at the history of the use of electric vehicles, it can be seen that they started to be used in the 1800s, but were not preferred at that time because the batteries could not match the range of internal combustion engines. At that time, the use of internal combustion engines was actually preferred due to a maximum range of 70 km and a speed limit of 40 km/h [11]. However, with the development of automotive and battery technology over the decades and the global warming that threatens the world in general every day, investment in electric vehicle technology and widespread use has increased. As a result of this positive discrimination in the development and use of electric vehicles, countries aiming to expand the use of these vehicles around the world have made this situation the main policy.

Electric vehicles, due to their operating characteristics, can provide significant benefits in many fields, especially environmental benefits by significantly reducing exhaust emissions [7, 12-14]. In order to make the use and operation of electric vehicles more effective and to fully reveal their positive effects, a large number of studies are being conducted worldwide. Most studies in this area focus on the widespread use of electric vehicles. Looking at the use of electric vehicles worldwide, it can be seen that three quarters of all new vehicles sold in 2021 will be electric vehicles [15]. On the other hand, it can be seen that this rate is quite low (2%) in the US in 2019 [15].

On the other hand, another important parameter for the widespread use of electric vehicles is charging facilities. The number of charging points has a very important role to play in increasing the use of electric vehicles. Studies on EV charging infrastructure have been carried out in many different countries. For example, according to a study conducted by [16] in China, access to charging stations in public places is shown to be the most important factor in people's adoption of EVs. According to another study conducted in the US, the lack of charging stations for EVs was identified as the most important barrier for society to adopt and use these vehicles [17]. In Norway, where the rate of EV use is quite high, [18] found that the availability of charging facilities is an important factor in consumers' decision making. In addition to charging station infrastructure, consumer expectations and behaviour, i.e., driver acceptance of these new vehicle types, are also highly influential in their diffusion. In the UK, [19] investigated the impact of incentives on electric vehicle (EV) sales using empirical evidence. In this context, [19] collected data on EV sales and incentives in the UK between 2011 and 2018 and analyzed the relationship between the variables. The results showed that incentives have a positive and significant impact on EV sales in the UK. In addition, the study found that the impact of incentives on EV sales varies across regions and income groups. Overall, the study suggests that government incentives can be an effective policy tool to encourage EV uptake, but their effectiveness may depend on the specific context and details of implementation.

In addition to charging infrastructure and consumer choice and behaviour, environmental factors play a very important role in the widespread use of electric vehicles. In this context, there have been many studies investigating the environmental benefits of electric vehicles compared to fossil-fuelled vehicles. [20] found that electric vehicles have a significantly lower carbon footprint than internal combustion vehicles. Another study compared electric vehicles with fossil-fuelled vehicles in China and found that electric vehicles play an important role in reducing air pollution compared to other vehicle types [21]. On the other hand, in a comprehensive study conducted in the European Union, [22] found that a switch to electric vehicles could reduce greenhouse gas emissions by almost 90% by 2050. The study found that although there are delays in implementation across Europe, the effect of the switch will bring vehicle-related greenhouse gas emissions close to net zero by the 2050s. The aim is to ensure the continuity of a habitable world by reducing air pollution factors to zero in a short time in a world where global warming is increasing day by day.

It is very important to plan systematic and operational preparations in advance in university campuses that will be pioneers in the use of electric vehicles in Türkiye. In this study, the required charging stations for fully electric vehicles for Ondokuz Mayıs University Kurupelit Campus (Central Campus) in Samsun, where major investments are being made in Smart City and Intelligent Transportation Systems (ITS), were designed according to the existing traffic density, parking capacity and density. In this context, the feasibility study determined how many charging stations should be placed in the existing car parks according to different percentages of electric vehicle use within the campus. In this respect, the study proposed a planning method that shows how the number of charging points will change depending on the use of electric vehicles on the campus and where they should be placed. By applying the method proposed in the study to other campuses, it is predicted that universities in Türkiye will be a pioneering example in the transition of universities to electric vehicles. In this way, universities will be able to observe the problems of the transition in advance and identify the problems that may occur in advance. Thus, they will be able to develop solutions to the identified problems in advance.

## 2. Current Situation in the e-Vehicle Market

### 2.1. Current situation in the world

Analyzing the available statistics on the number of electric vehicles, the cumulative number of electric vehicles in China reached 260 thousand by the end of 2019. Meanwhile, the total number of charging stations reached 65,000. Similarly, in Paris, London and Amsterdam, one of the leading cities in Europe, the cumulative number of electric vehicles reached 40 thousand and the number of charging stations reached 4 thousand, 6 thousand and 10 thousand respectively. In Oslo, the capital of Norway, which has the highest rate of electric vehicle use in the world, the number of electric vehicles reached 110,000 and the number of charging stations reached 5,000 [3]. In Los Angeles, the three largest electric vehicle markets in the world, this number has reached 200 thousand, 120 thousand in San Jose and 100 thousand in San Francisco. The number of charging stations was found to have reached 2 thousand in San Jose, 3 thousand in San Francisco and 5 thousand in Los Angeles [23].

China stands out as one of the world's largest markets for electric vehicle sales. Even surpassing the US, China alone sells 46% of all electric cars sold worldwide. In addition, around 43% of the electric cars produced in 2020 will be made by Chinese carmakers [24]. In Europe, electric vehicle sales are not as high as in the US and China. The main reason for this is that the EU's incentives for electric cars are not as effective as in the US and China (Fig. 1).

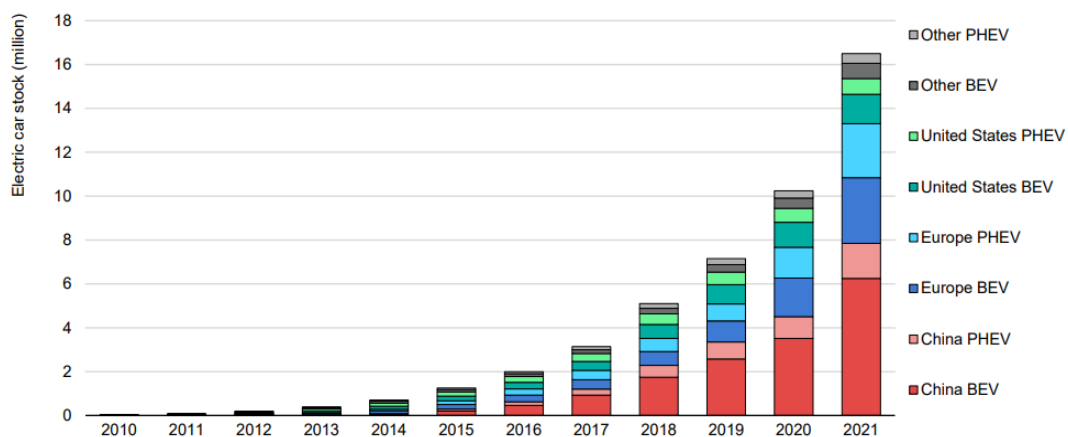


Fig. 1. The number of existing vehicles in the world in 2021 and the change by Years [24]



## 2.2. Current situation in Türkiye

According to the report prepared by TEHAD, the interest in electric cars in Türkiye is not at the desired level. Currently, the number of electric vehicles is around 6,500-7,000 (excluding hybrid vehicles). However, there has been a significant increase in electric car sales in recent years. For example, analysing the sales figures for the first six months of 2022, a total of 2413 electric vehicles were sold. This figure is significantly higher than the 894 units sold in the same period last year (Fig. 2). It is therefore expected that a total of more than 4,000 electric vehicles will be sold by the end of 2022. This figure represents an almost threefold increase (Fig. 2) [25].

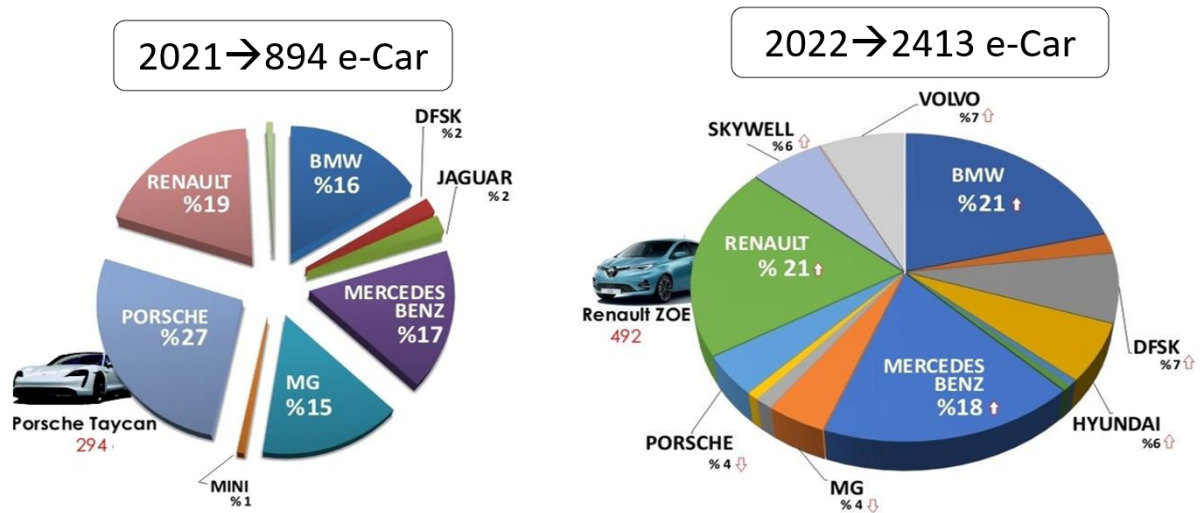


Fig. 2. Change in electric vehicle sales in Türkiye [25]

The domestic electric vehicle production and development process in Türkiye started with the production of solar-powered vehicles at METU in 2003. Later, the production of electric vehicles, which started in other universities, developed further with ITU receiving serious support from universities. In addition to universities, car companies have also started electric car production in Türkiye. For example, Renault produced the electric model 'Fluance' at its Bursa plant in 2011 and tested it in Europe for a long time. The Koç Group has also developed electric cars under the Ford "Focus" brand, but has not been able to start mass production due to infrastructure problems in Türkiye. Similarly, Toyota has also produced electric vehicles, but has not been able to start mass production due to infrastructure problems for the use of electric vehicles in Türkiye [25].

Nowadays, electric vehicles have started to be actively used in many countries of the world, especially in European countries, by establishing infrastructure systems and electric charging stations. In Türkiye, a large number of studies have been carried out in this field in recent years. As the market share in this field is quite high, the interest in this field is quite high. Studies in many areas such as batteries, charging stations, etc., especially for electric cars, minibuses and buses, are actively continuing (Fig. 3).

In 2017, a vision plan was announced to produce Türkiye's first domestic electric car. A year later, a consortium consisting of Anadolu Group (19%), BMC (19%), Kök Group (19%), Türkcell (19%), Zorlu Holding (19%) and TOBB (5%) was formed, resulting in the establishment of Türkiye's Automobile Initiative Group Industry and Trade Inc. on 25 June 2018. TOGG presented the SUV and sedan models of the domestic car at a press conference on 27 December 2019, and a factory was built in Gemlik as part of this production. The factory was opened on 29

October 2022 and mass production started with the first mass-produced vehicle coming off the line (Fig. 4).



Fig. 3. Sample images of some ongoing electric vehicle studies [25]



Fig. 4. Sample images of the domestic car TOGG SUV model and images of the vehicles planned to be produced [26]

In addition to the electric car, Türkiye's leading domestic bus manufacturers BMC, Otocar, Temsa, Karsan, Bozankaya and Akia have developed electric bus designs and started production. Many of these companies now offer their domestic buses for use in public transport in both domestic and international markets.

### 2.3. Availability of car parks as charging stations

While there were around 2,500 electric vehicles in Türkiye at the end of 2017, the aim was to increase this number to 140,000 within four years. In addition, 14,000 commercial and 70,000 residential charging units were to be installed. However, these targets have not been met over the years. For 2022, the target has been set at 140,000 electric vehicles and 14,000 commercial charging units. With the existing infrastructure, 25 per cent of the 14,000 charging units should be DC fast charging units and the rest AC charging units. In addition, the number of residential charging units is expected to be around 70 thousand, but unfortunately these numbers have not been reached [27, 28]. Although there has been a significant increase in the number of electric vehicles in Türkiye in recent years, unfortunately it is far from the desired targets (Fig. 5).



Fig. 5. Location map of available charging stations in Türkiye [25]

There are currently around 4,000 charging stations in Türkiye. However, it is expected that the number of electric vehicles charging stations will reach tens of thousands in a short period of time after the Turkish domestic car TOGG starts mass production. With the launch of the TOGG domestic electric vehicle, many companies in Türkiye are expected to use electric vehicles in their fleets. Currently, Türkiye ranks last among the countries with charging stations in Europe, but this number is expected to increase very quickly with the TOGG Trugo developed for the domestic car TOGG [7]

When analysing the locations of electric vehicles in Türkiye in Fig. 5, it can be seen that the number of electric vehicles charging stations is quite insufficient. The most appropriate solution proposed to solve this problem is to use existing urban and intercity car parks as electric vehicle charging stations (Fig. 6). However, it is important to take traffic density into account when designing charging points and to install charging points accordingly. In the future, it is envisaged that all car parks will be fully used as charging stations. It is therefore very important and necessary to develop a new management system and to adapt the existing car parks to this system.



Fig. 6. Existing car parks as potential charging stations [29]

Placing charging stations only in existing indoor and outdoor car parks, and not analysing capacity utilisation and operational performance according to this new situation, may lead to long queues of vehicles and complexities at the entrance and exit of these car parks in the near future (Fig. 7).



Fig. 7. Queue formations which poorly designed and planned parking lots [30]

The following flow chart summarises the steps that need to be taken in order to avoid this problem in the pilot area (Fig. 8).

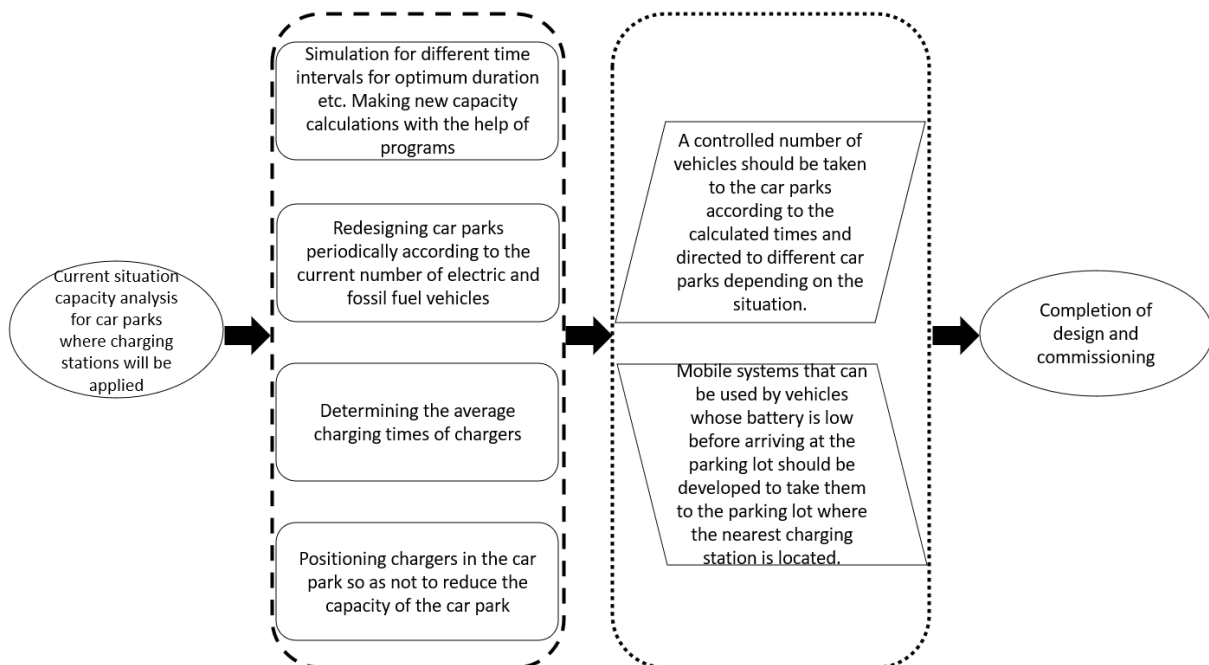


Fig. 8. Workflow plan for what to do in parking lot design for electric vehicles

### 3. Ensuring the Use of Zero Emission Vehicles in Omu Kurupelit Campus

#### 3.1. Information about OMU campus

Ondokuz Mayıs University Kurupelit Campus covers an area of 10,000 hectares. There are many faculties, units and hospitals on the campus. Visuals of the campus are shown in Fig. 9.



Fig. 9. Image of OMÜ Kurupelit Campus [31]

The Kurupelit campus can be reached by tram, bus and minibus. Looking at the statistics for 2022, a total of 53201 students are studying at Ondokuz Mayıs University. 2524 academic staff and 3977 administrative staff support the education and training activities. In order to spread the use of zero-emission electric vehicles, which have become widespread in the world, in the central campus of OMU, it has been tried to make suggestions for the creation of infrastructure for the widespread use of electric vehicles according to the existing traffic parameters and parking facilities on the campus

### 3.2. Determining the amount of campus traffic

As part of the research, an attempt was made to determine the amount of existing traffic flow on the campus. To do this, the images from the security cameras at the main entrance and exit to the campus were analysed in a computer environment using a special coding language and image processing (Fig. 10).

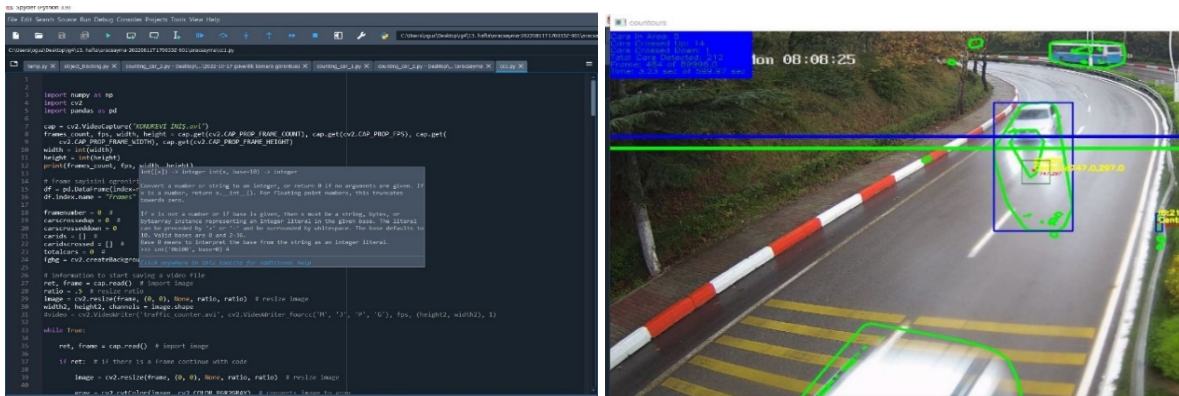


Fig. 10. Determination of traffic amount after analysis of camera images with image processing

At this stage, the most active period of vehicle mobility at the university was selected and the busiest periods were analysed as much as possible. Based on the data obtained from the image processing analysis in the computer environment, the current average daily traffic at the campus entrance was obtained according to vehicle-based time zones as shown in Table 1.

Table 1. Average number of available vehicles by type for OMU Kurupelit campus

Time Interval	Vehicle Type					Total
	Passenger Car	Van	Bus	Truck	Lorry	
0-1	111	23	0	11	0	144
1-2	58	14	0	7	0	78
2-3	38	8	0	8	0	54
3-4	32	8	0	8	0	48
4-5	16	2	0	2	0	21
5-6	19	6	0	4	0	30
6-7	48	11	10	16	0	86
7-8	276	78	17	65	2	440
8-9	560	101	20	86	6	774
9-10	737	149	14	63	11	975
10-11	938	162	12	89	7	1208
11-12	1308	203	10	69	16	1606
12-13	1054	182	13	76	19	1345
13-14	813	111	15	75	8	1022
14-15	1179	168	12	82	15	1456
15-16	1490	226	12	86	22	1836
16-17	1936	334	15	94	33	2411
17-18	1065	191	20	80	16	1372
18-19	548	94	20	62	7	730
19-20	513	61	19	51	6	650
20-21	324	52	16	53	4	449
21-22	262	39	14	44	3	360
22-23	211	38	8	23	1	281
23-24	213	35	1	19	0	268
07-19	11904	2000	180	929	163	15176
06-22	13051	2163	239	1092	176	16720
06-00	13475	2235	248	1134	177	17269
00-00	13748	2297	248	1174	177	17644

The results shown in Fig. 11 are obtained by analysing the hourly distribution of the average daily traffic flow values obtained.

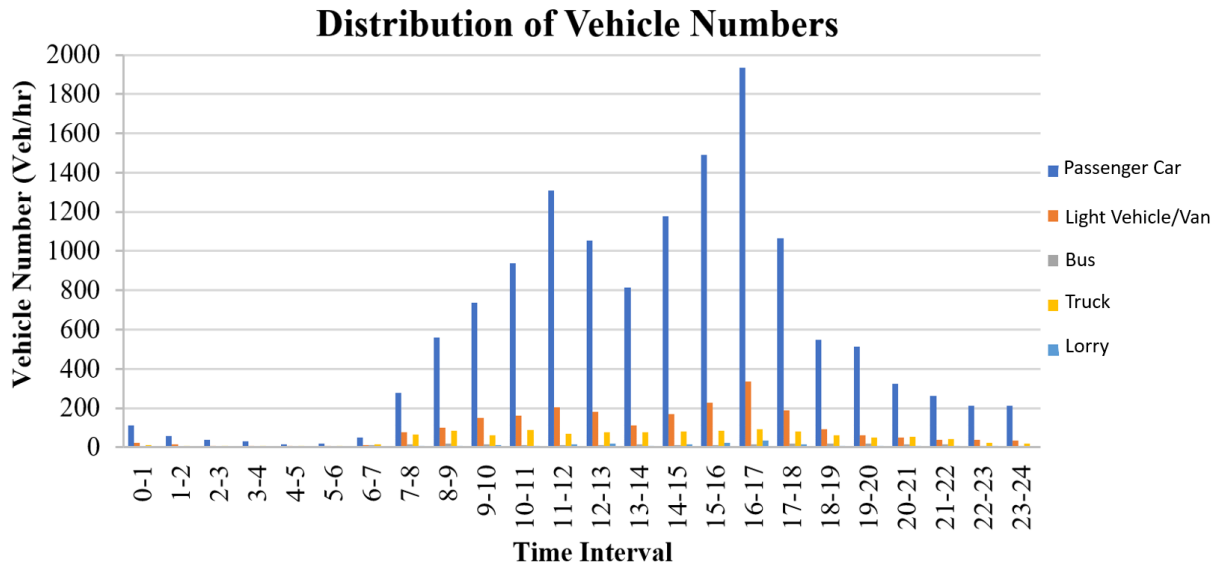


Fig. 11. Hourly distribution of current average traffic on campus by vehicle types

The distribution of the traffic on the campus according to certain time intervals and types of vehicles is shown in Fig 12.

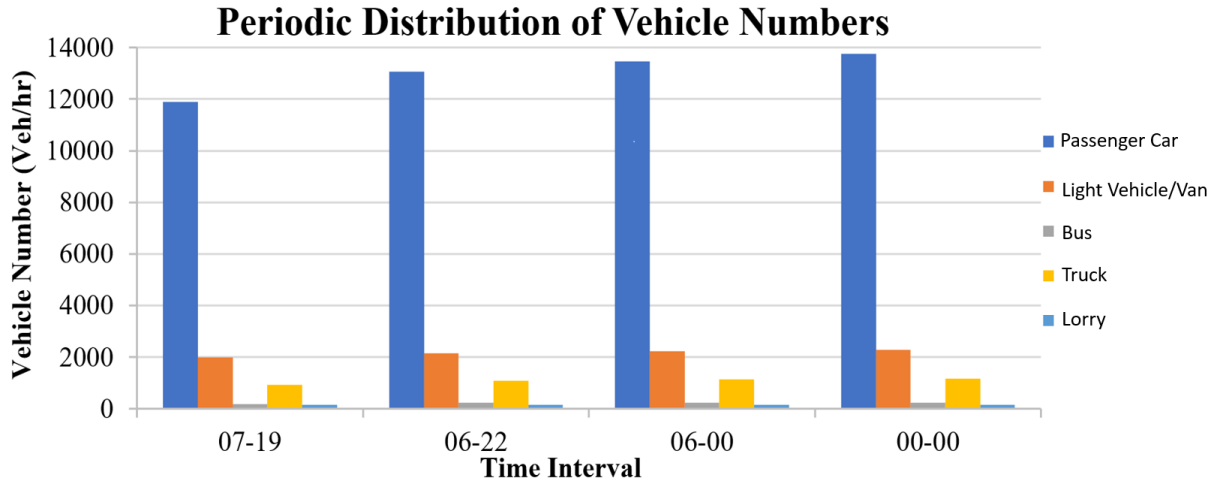


Fig. 12. Distribution of current average traffic on campus according to certain period intervals

An analysis of Figure 12 shows that most of the vehicles accessing the campus are distributed between 07:00 and 19:00. According to the average number of vehicles obtained, 15 thousand vehicles access the campus between these hours and 17 thousand vehicles on a daily basis.

### 3.3. Examination of the existing car parking capacity and parking lot usage on campus

In order to determine the existing car parking capacity and the average usage rate (average occupancy percentage) of these car parks on the Kurupelit campus, all actively used car parks on the campus were first mapped and grouped by number. The study of the capacity and use of the car parks included only the areas designed as car parks, not the street parking areas. The next step was to carry out field inspections to determine the capacity and average occupancy of all car parks, and to transfer and digitize the data obtained into the computer environment (Fig. 13).



Fig. 13. Collection of field data of parking lots

Table 2. The occupancy rate and capacity data of the car parks obtained by field observations

Location-Car Park No	Average Current Vehicle Number	Capacity (Vehicle)	Average Occupancy (%)
1- OMÜ Koleji Car Park	23	76	30.3
2- OMÜ Rektörlük Otopark-2	32	44	72.7
3- OMÜ Rektörlük Car Park-1	45	78	57.7
4- OMÜ AKM Car Park	72	85	84.7
5- OMÜ Hastanesi Car Park-5	185	235	78.7
6- OMÜ Tıp Fakültesi Car Park	23	24	95.8
7- OMÜ Hastanesi Car Park-6	27	29	93.1
8- OMÜ Hastanesi Kapalı Car Park-1	140	185	75.7
9- OMÜ Tıp Dekanlık Car Park	105	150	70.0
10- OMÜ Hastanesi Car Park-4	47	50	94.0
11- OMÜ Hastanesi Car Park-3	70	87	80.5
12- OMÜ Hastanesi Car Park-2	38	45	84.4
13- OMÜ Hastanesi Car Park-1	582	1200	48.5
14- OMÜ Hastanesi Car Park-9	49	114	43.0
15- OMÜ Hastanesi Car Park-8	38	44	86.4
16- OMÜ Veteriner Fakültesi Car Park-1	15	18	83.3
17- OMÜ Diş Hekimliği Car Park-1	122	158	77.2
18- OMÜ Diş Hekimliği Car Park-3	100	110	90.9
19- OMÜ Spor Bilimleri Fakültesi Car Park-1	5	16	31.3
20- OMÜ Tömer Otopark-2	16	34	47.1
21- OMÜ Spor Bilimleri Fakültesi Otopark-2	15	24	62.5
22- OMÜ Tömer Otopark-1	12	39	30.8
23- OMÜ Spor Bilimleri Fakültesi Otopark-3	61	84	72.6
24- OMÜ Spor Bilimleri Fakültesi Otopark-4	13	14	92.9
25- OMÜ Tömer Car Park-3	16	40	39.5
26- OMÜ Veteriner Fakültesi Car Park-2	47	62	75.8
27- OMÜ Hastanesi Car Park-10	43	35	122.9
28- OMÜ Hastanesi Car Park-7	59	65	90.8
29- OMÜ Hastanesi Kapalı Car Park-2	541	517	104.6
30- OMÜ Cami Car Park	6	56	10.7
31- OMÜ Diş Hekimliği Car Park-2	32	48	66.7
32- OMÜ İlahiyat Fakültesi Car Park	46	63	73.0
33- OMÜ UZEM Car Park	56	98	57.1
34- OMÜ KYK Yurdu Car Park	35	37	94.6
35- OMÜ İİBF Car Park	4	12	33.3
36- OMÜ Sağlık Bilimleri Fakültesi Car Park	70	88	79.6
37- OMÜ Merkez Kütüphane Car Park	12	96	12.5
38- OMÜ Ziraat Fakültesi Car Park	96	163	58.9
39- OMÜ Hayvan Hastanesi Car Parkları	34	53	64.2
40- OMÜ Eğitim Fakültesi Car Park	61	150	40.7
41- OMÜ Fen-Edebiyat Fakültesi Car Parkları	221	550	40.2
42- OMÜ Veteriner Car Park-3	43	60	72.1
43- OMÜ Yaşam Merkezi Car Park	43	70	61.4
44- OMÜ Mühendislik Fakültesi Car Parkları	130	224	58.0
45- OMÜ Teknopark Car Park	21	45	46.7
<b>Total (Σ)</b>	<b>3241</b>	<b>5436</b>	<b>Avg. 66.4</b>

As part of the field observations and analysis, the car parks that can be used by electric vehicles on the Kurupelit campus were grouped (those close to each other were considered as a composite)



and a total of 45 car parks were identified, as shown in Fig. 14. The capacity and average occupancy rates of these car parks are shown in Table 2.

Table 3. The order of the existing car parks according to their capacities, from the largest to the smallest

No for the Capacity	Car Park No- Location	Capacity (Veh.)	Average Occupancy (%)
1	13- OMÜ Hastanesi Car Park-1	1200	48,5
2	41- OMÜ Fen-Edebiyat Fakültesi Car Parks	550	40.2
3	29- OMÜ Hastanesi Kapalı Car Park-2	517	104.6
4	5- OMÜ Hastanesi Car Park-5	235	78.7
5	44- OMÜ Mühendislik Fakültesi Car Parks	224	58.0
6	8- OMÜ Hastanesi Kapalı Car Park-1	185	75.7
7	38- OMÜ Ziraat Fakültesi Car Park	163	58.9
8	17- OMÜ Diş Hekimliği Car Park-1	158	77.2
9	9- OMÜ Tıp Dekanlık Car Park	150	70.0
10	40- OMÜ Eğitim Fakültesi Car Park	150	40.7
11	14- OMÜ Hastanesi Car Park-9	114	43.0
12	18- OMÜ Diş Hekimliği Car Park-3	110	90.9
13	33- OMÜ UZEM Car Park	98	57.1
14	37- OMÜ Merkez Kütüphane Car Park	96	12.5
15	36- OMÜ Sağlık Bilimleri Fakültesi Car Park	88	79.5
16	11- OMÜ Hastanesi Car Park-3	87	80.5
17	4- OMÜ AKM Car Park	85	84.7
18	23- OMÜ Spor Bilimleri Fakültesi Car Park-3	84	72.6
19	3- OMÜ Rektörlük Car Park-1	78	57.7
20	1- OMÜ Koleji Car Park	76	30.3
21	43- OMÜ Yaşam Merkezi Car Park	70	61.4
22	28- OMÜ Hastanesi Car Park-7	65	90.8
23	32- OMÜ İlahiyat Fakültesi Car Park	63	73.0
24	26- OMÜ Veteriner Fakültesi Car Park-2	61	72.1
25	42- OMÜ Veteriner Car Park-3	62	75.8
26	30- OMÜ Cami Car Park	56	10.7
27	39- OMÜ Hayvan Hastanesi Car Parkları	53	64.2
28	10- OMÜ Hastanesi Car Park-4	50	94.0
29	31- OMÜ Diş Hekimliği Car Park-2	48	66.7
30	12- OMÜ Hastanesi Car Park-2	45	84.4
31	45- OMÜ Teknopark Car Park	45	46.7
32	2- OMÜ Rektörlük Car Park-2	44	72.7
33	15- OMÜ Hastanesi Car Park-8	40	40.0
34	25- OMÜ Tömer Car Park-3	44	86.4
35	22- OMÜ Tömer Car Park-1	39	30.8
36	34- OMÜ KYK Yurdu Car Park	37	94.6
37	27- OMÜ Hastanesi Car Park-10	35	122.9
38	20- OMÜ Tömer Car Park-2	34	47.1
39	7- OMÜ Hastanesi Car Park-6	29	93.1
40	6- OMÜ Tıp Fakültesi Car Park	24	95.8
41	21- OMÜ Spor Bilimleri Fakültesi Car Park-2	24	62.5
42	16- OMÜ Veteriner Fakültesi Car Park-1	18	83.3
43	19- OMÜ Spor Bilimleri Fakültesi Car Park-1	16	31.3
44	24- OMÜ Spor Bilimleri Fakültesi Car Park-4	14	92.9
45	35- OMÜ İİBF Car Park	12	33.3
<b>Total (Σ)</b>		<b>5436</b>	<b>Avg. 66.4</b>

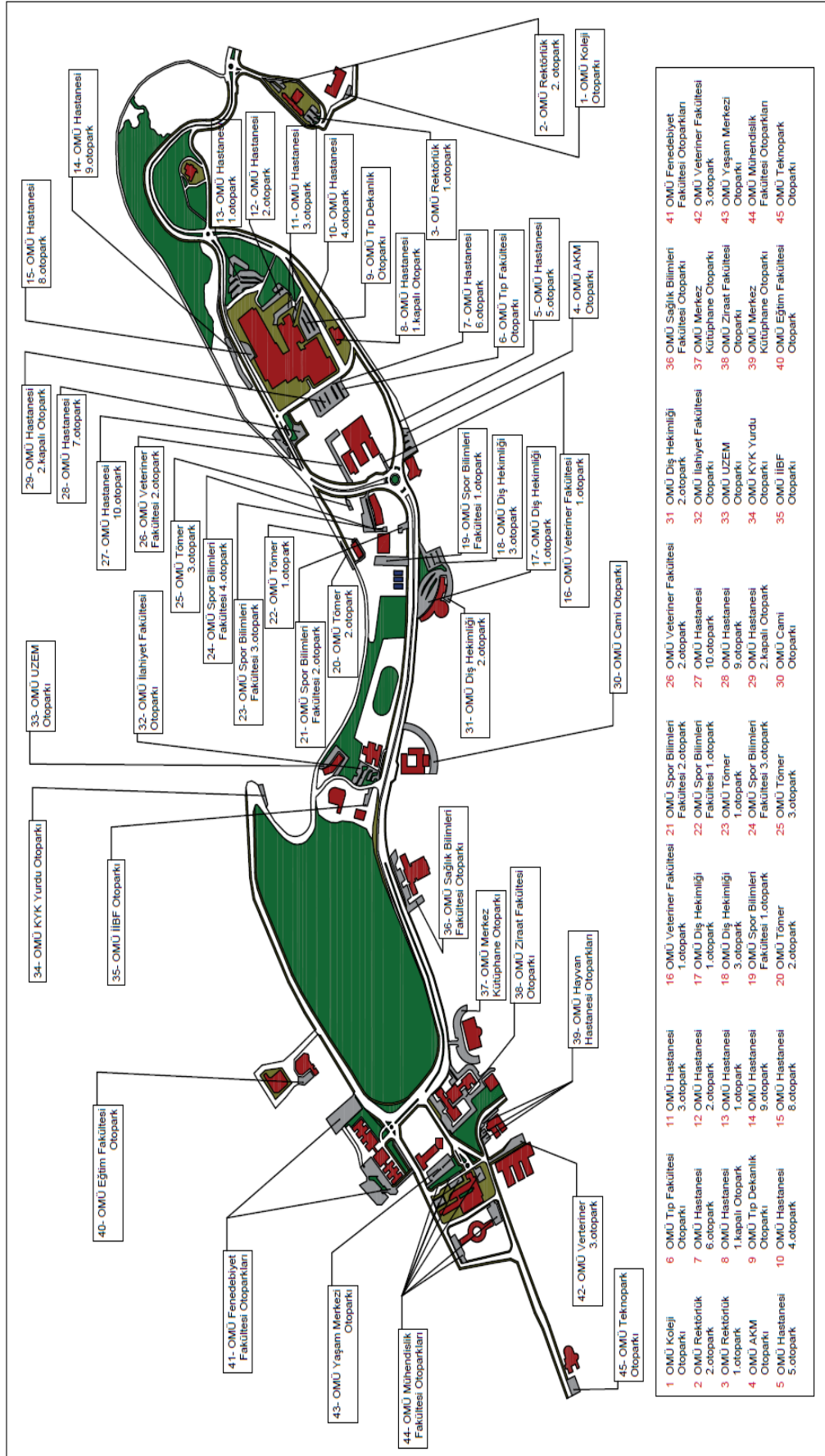


Fig. 14. Existing car parks on the OMU Kurupelit campus

From the car park capacity analysis, it was found that the average occupancy rate of the car parks within the university is 66.4%. To determine the location and number of EV charging points in the existing car parks, the existing car parks were ranked according to their capacity and occupancy rates, with priority given to those with the highest capacity (Table 3).

There are many important parameters in determining the number of charging stations, which is the most important issue in the use of electric vehicles. As it is known, electric cars, electric light commercial vehicles (pick-up trucks, minibuses and vans) and electric buses are the vehicles in the forefront, as they are at the beginning of the process of spreading electric vehicles today. Therefore, the number of charging stations in the OMU Kurupelit campus has been determined by taking these issues into consideration when making effective planning. Since the use of electric buses and the necessary work on charging stations is being carried out by Samsun Metropolitan Municipality in this planning, no planning work has been carried out for electric buses at the moment. In this study, a calculation was made and a proposal was developed for the location and number of charging stations for electric cars and electric light commercial vehicles (vans, minibuses and light commercial vehicles). In this context, it is very important to develop cost-effective proposals by carefully examining all parameters when determining the number of these expensive systems for the widespread use of electric vehicles. In the study, when determining the number of vehicles entering the campus (for two types), the total number of vehicles (13904) between 07:00 and 19:00, when the highest density is observed, was taken into account. In this context, the calculations

- Total number of vehicles on campus (day)
- Parking capacity (vehicle)
- Occupancy rate (%)
- Average number of vehicles in the car park
- Percentage availability of electric vehicles (1%, 5%, 10% and 25%)
- The total car parking capacity (vehicles) on campus was taken into account as a calculation parameter.

Taking all these parameters into account, the study calculated the number of charging stations according to different percentage scenarios, depending on the campus-specific situation, using the relationship given in Equation 1, and the results are shown in Table 4.

$$N_{CS} = \left[ (EV\% \times N_{TV}) \times \frac{N_{EP}}{N_{TCP}} \right] * \left( \frac{N_{ACP}}{N_{EP}} \right) \quad (1)$$

Where  $N_{CS}$  is charging station number,  $EV\%$  is e-Vehicle percentage (%1, %5, %10 ve %25),  $N_{TV}$  is total vehicle number in the campus for passenger car and light vehicles/vans,  $N_{EP}$  is examined car park capacity,  $N_{TCP}$  is total car park capacity in the campus and  $N_{ACP}$  is average vehicle numbers for the examined car park.

The distribution of the number of EV charging points recommended according to the number of EVs in the identified percentage scenarios by car parks is shown in detail in Fig. 15 (a-o). According to the results of the analyses, it is recommended to install the number of EV charging points shown in Fig. 15 (a-o) when the percentage of EVs specified in the scenarios is reached with the gradual diffusion of the domestic electric car TOGG.

Table 4. The number of e-charging stations recommended for car parks according to the percentage distribution of the number of e-vehicles in traffic (1%, 5%, 10% and 25%)

No for the Capacity	Car Park No- Location	Capacity (Veh.)	Average Occupancy (%)	Total Number of Charging Stations for Electric Vehicle Percentage			
				1%	5%	10%	25%
1	13- OMÜ Hastanesi Car Park-1	1200	48.5	15	74	149	372
2	41- OMÜ Fen-Edebiyat Fakültesi Car Parkları	550	40.2	6	28	57	141
3	29- OMÜ Hastanesi Kapalı Car Park-2	517	104.6	14	69	138	346
4	5- OMÜ Hastanesi Car Park-5	235	78.7	5	24	47	118
5	44- OMÜ Mühendislik Fakültesi Car Park	224	58.0	3	17	33	83
6	8- OMÜ Hastanesi Kapalı Car Park-1	185	75.7	4	18	36	90
7	38- OMÜ Ziraat Fakültesi Car Park	163	58.9	2	12	25	61
8	17- OMÜ Dış Hekimliği Car Park-1	158	77.2	3	16	31	78
9	9- OMÜ Tıp Dekanlık Car Park	150	70.0	3	13	27	67
10	40- OMÜ Eğitim Fakültesi Car Park	150	40.7	2	8	16	39
11	14- OMÜ Hastanesi Car Park-9	114	43.0	1	6	13	31
12	18- OMÜ Dış Hekimliği Car Park-3	110	90.9	3	13	26	64
13	33- OMÜ UZEM Car Park	98	57.1	1	7	14	36
14	37- OMÜ Merkez Kütüphane Car Park	96	12.5	0	2	3	8
15	36- OMÜ Sağlık Bilimleri Fakültesi Car Park	88	79.5	2	9	18	45
16	11- OMÜ Hastanesi Car Park-3	87	80.5	2	9	18	45
17	4- OMÜ AKM Car Park	85	84.7	2	9	18	46
18	23- OMÜ Spor Bilimleri Fakültesi Car Park-3	84	72.6	2	8	16	39
19	3- OMÜ Rektörlük Car Park-1	78	57.7	1	6	12	29
20	1- OMÜ Koleji Car Park	76	30.3	1	3	6	15
21	43- OMÜ Yaşam Merkezi Car Park	70	61.4	1	5	11	27
22	28- OMÜ Hastanesi Car Park-7	65	90.8	2	8	15	38
23	32- OMÜ İlahiyat Fakültesi Car Park	63	73.0	1	6	12	29
24	26- OMÜ Veteriner Fakültesi Car Park-2	61	72.1	1	6	11	28
25	42- OMÜ Veteriner Car Park-3	62	75.8	1	6	12	30
26	30- OMÜ Cami Car Park	56	10.7	0	1	2	4
27	39- OMÜ Hayvan Hastanesi Car Parkları	53	64.2	1	4	9	22
28	10- OMÜ Hastanesi Car Park-4	50	94.0	1	6	12	30
29	31- OMÜ Dış Hekimliği Car Park-2	48	66.7	1	4	8	20
30	12- OMÜ Hastanesi Car Park-2	45	84.4	1	5	10	24
31	45- OMÜ Teknopark Car Park	45	46.7	1	3	5	13
32	2- OMÜ Rektörlük Car Park-2	44	72.7	1	4	8	20
33	15- OMÜ Hastanesi Car Park-8	44	86.4	1	5	10	24
34	25- OMÜ Tömer Car Park-3	40	40.0	0	3	5	13
35	22- OMÜ Tömer Car Park-1	39	30.8	0	2	3	8
36	34- OMÜ KYK Yurdu Car Park	37	94.6	1	4	9	22
37	27- OMÜ Hastanesi Car Park-10	35	122.9	1	5	11	27
38	20- OMÜ Tömer Car Park-2	34	47.1	0	2	4	10
39	7- OMÜ Hastanesi Car Park-6	29	93.1	1	3	7	17
40	6- OMÜ Tıp Fakültesi Car Park	24	95.8	1	3	6	15
41	21- OMÜ Spor Bilimleri Fakültesi Car Park-2	24	62.5	0	2	4	10
42	16- OMÜ Veteriner Fakültesi Car Park-1	18	83.3	0	2	4	10
43	19- OMÜ Spor Bilimleri Fakültesi Car Park-1	16	31.3	0	1	1	3
44	24- OMÜ Spor Bilimleri Fakültesi Car Park-4	14	92.9	0	2	3	8
45	35- OMÜ İİBF Car Park	12	33.3	0	1	1	3
Total (Σ)		5436	Avg. 66.4	88	442	884	2210

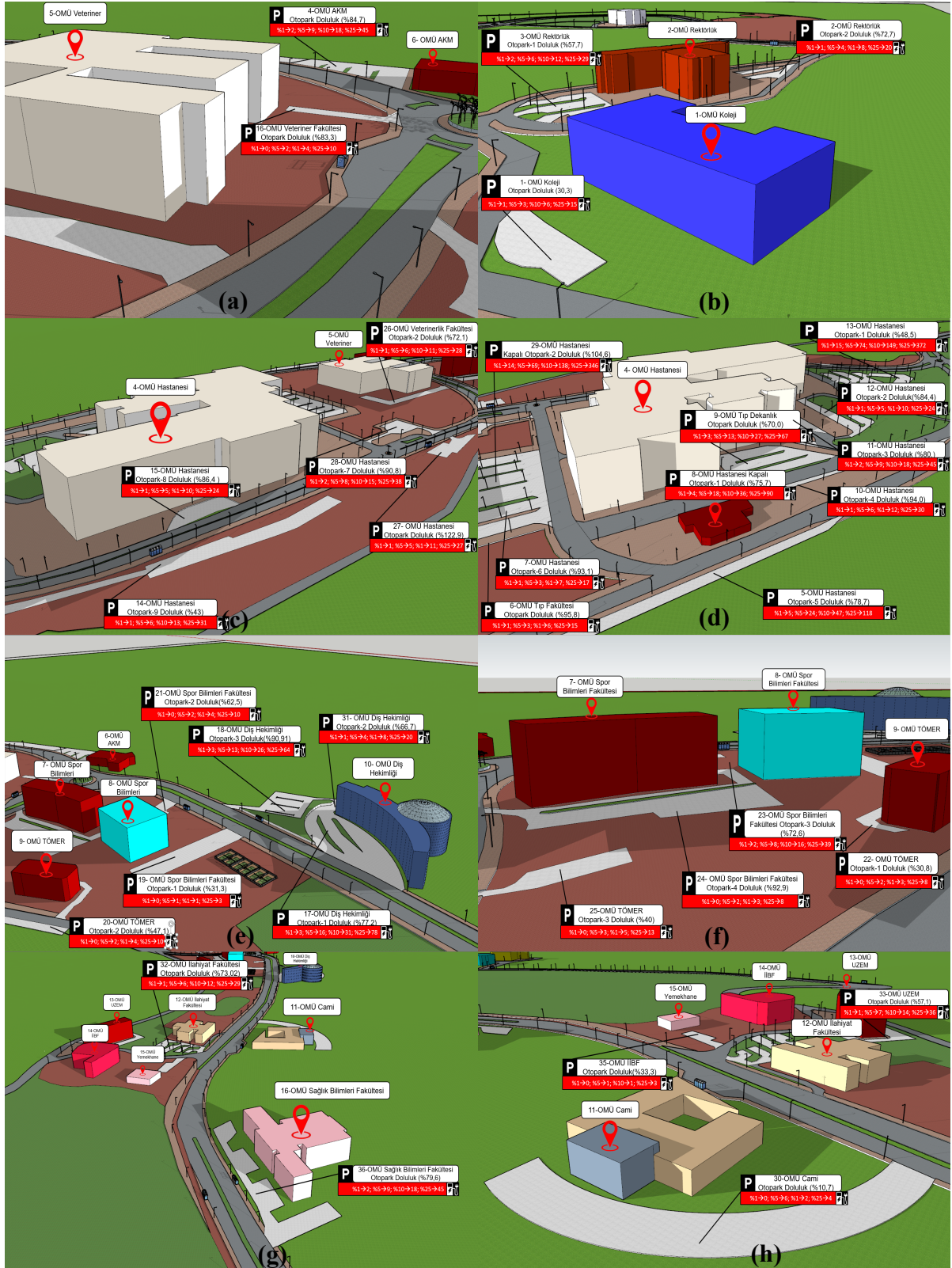




Fig. 15. Distribution of charging stations in car parks obtained as a result of calculations according to e-vehicle percentage scenarios (a-o)

#### 4. Conclusion and Recommendations

Ongoing research around the world shows that technological research for the development of electric vehicles and incentives for their widespread use are continuing at the usual pace, and efforts are being made for the effective use of electric vehicles on all roads. At present, the main obstacle to the preference of electric vehicles in Türkiye is the lack of sufficient charging (e-charging) stations to ensure fast charging of vehicles. This study examines the current number of active vehicles on campus and proposes electric vehicle charging stations (in terms of location and number) in the campus car parks according to electric vehicle percentage scenarios. Thus, this study will be a guideline for the use of e-charging stations within the central campus of Ondokuz Mayıs University in 2023 and beyond, when the use of electric vehicles will become more widespread in our country with the domestic e-vehicle "TOGG". OMU Kurupelit campus will be a pioneer campus in the use of electric vehicles with the implementation of the proposed locations and number of charging stations when the identified scenarios are realised. All charging stations proposed in this study are designed for fast charging (~20-45 min) instead of slow charging (~8 hours) in the campus where vehicle and parking mobility is intense. There are large transformers and sub-centres within the OMU central campus and it is envisaged that this situation will work effectively even if the vehicles consume high current electricity. Again, before installing charging stations, it is necessary to evaluate the issue in terms of electrical power and transformer capacity, assuming that vehicles can charge at the same time.

The study believes that the steps to be taken for the use of electric vehicles on campus and their charging needs will bring the importance and use of electric vehicles to the forefront of our country's 2023 visions and will further increase the demand for the domestic electric car (TOGG), which will enter the production phase. The ability to charge their EVs on campus, especially for academics, administrative staff, students and guests who spend most of their day on the university campus, will be an incentive for them to use EVs and for OMU to become a green campus university. It is expected that universities will be able to take an active role in the use and operation of electric vehicles when similar studies are carried out in other university campuses.

#### Acknowledgments

This study was conducted under a research project titled "i-gCar4ITS: Innovative and Green Carrier Development for Intelligent Transportation System Applications" which was supported by British Council. The authors would like to thank British Council for this support.

#### Notations

$N_{CS}$	Charging station number
$EV\%$	e-Vehicle percentage (%1, %5, %10 ve %25)
$N_{TV}$	Total vehicle number in the campus for passenger car and light vehicles/vans
$N_{EP}$	Examined car park capacity
$N_{TCP}$	Total car park capacity in the campus
$N_{ACP}$	Average vehicle numbers for the examined car park

#### References

- [1] Abid, M., Tabaa, M., Chakir, A., Hachimi, H., Routing and charging of electric vehicles: Literature review. *Energy Reports*, 8, 556-578, 2022.
- [2] Oladunni, O. J., Mpofu, K., Olanrewaju, O. A., Greenhouse gas emissions and its driving forces in the transport sector of South Africa. *Energy Reports*, 8, 2052-2061, 2022.

- [3] Aydın, M. M., Çakmak, R., & Yıldırım, M. S., Şehiriçi otoparklarda elektrikli araç şarj istasyonlarının kurulumu için gerekli tasarım aşamalarının belirlenmesi. In *International Congress on Engineering and Architecture*, Nov. 14-16, 2018, (pp. 900-915), Alanya, Türkiye.
- [4] Aydın, M. M., Köfteci, S., Koridor Ortalama Hız İhlal Tespit Sistemlerinin (KOHİTS) Tasarımdan İşletmeye Genel Yapısı ve Çalışma Prensipleri Üzerine Bir Araştırma: Toprakkale Örneği. *Gümüşhane Üniversitesi Fen Bilimleri Dergisi*, 10(1), 109-121, 2020.
- [5] Aydın, M. M., Köfteci, S., Akgöl, K., Yıldırım, M. S., Utilization of a new methodology on performance measurements of redlight violations detection systems. *International Journal of Engineering and Applied Sciences*, 9(1), 32-41, 2017.
- [6] Amjad, M., Ahmad, A., Rehmani, M. H., Umer, T., A review of EVs charging: From the perspective of energy optimization, optimization approaches, and charging techniques. *Transportation Research Part D: Transport and Environment*, 62, 386-417, 2018.
- [7] Çakmak, R., Aydın, M. M., & Yıldırım, M. S., Elektrikli araç şarj istasyonlarının elektrik şebekesi, elektrikli araç teknolojileri. In *International Congress on Engineering and Architecture*, Nov. 14-16, 2018, (pp. 916-930), Alanya, Türkiye.
- [8] Bıyık, B., Aydın, M. M., Dijital sistemler ve nesnelerin interneti tabanlı yeni bir akıllı otopark sistemi: bir kavramsal tasarım. *Gümüşhane Üniversitesi, Fen Bilimleri Enstitüsü Dergisi*, 13(4), 990-1008, 2023.
- [9] Ogunkunle, O., Ahmed, N. A., A review of global current scenario of biodiesel adoption and combustion in vehicular diesel engines. *Energy Reports*, 5, 1560-1579, 2019.
- [10] Subramaniam, M., Solomon, J. M., Nadanakumar, V., Anaimuthu, S., Sathyamurthy, R., Experimental investigation on performance, combustion and emission characteristics of DI diesel engine using algae as a biodiesel. *Energy Reports*, 6, 1382-1392, 2020.
- [11] Alanazi, F., Electric Vehicles: Benefits, Challenges, and Potential Solutions for Widespread Adaptation. *Applied Sciences*, 13(10), 6016, 2023.
- [12] Aydın, M. M., Aydoğdu, İ., & Yıldırım, M. S., Sinyalize kavşaklarda ülkelere göre gecikme ve kuyruk uzunluğu denklemleri geliştirilmesinin gerekliliği üzerine bir araştırma. *Gümüşhane Üniversitesi Fen Bilimleri Dergisi*, 12(2), 597-613, 2022.
- [13] Liu, D., Xu, L., Sadia, U. H., Wang, H., Evaluating the CO2 emission reduction effect of China's battery electric vehicle promotion efforts. *Atmospheric Pollution Research*, 12(7), 101115, 2021.
- [14] Sheng, M. S., Sreenivasan, A. V., Sharp, B., Du, B., Well-to-wheel analysis of greenhouse gas emissions and energy consumption for electric vehicles: A comparative study in Oceania. *Energy Policy*, 158, 112552, 2021.
- [15] International Energy Agency (IEA) *Global EV Outlook 2021: Accelerating the transition to electric vehicles*, [Online]. Available: <https://www.iea.org/reports/global-ev-outlook-2021>. [Accessed: Apr. 04, 2023], 2021.



- [16] Peng, Y., Bai, X., What EV users say about policy efficacy: Evidence from Shanghai. *Transport Policy*, 132, 16-26, 2023
- [17] Sierzchula, W., Bakker, S., Maat, K., Van Wee, B., The influence of financial incentives and other socio-economic factors on electric vehicle adoption. *Energy Policy*, 68, 183-194, 2014.
- [18] Visaria, A. A., Jensen, A. F., Thorhauge, M., Mabit, S. E., User preferences for EV charging, pricing schemes, and charging infrastructure. *Transportation Research Part A: Policy and Practice*, 165, 120-143, 2022.
- [19] Helveston, J. P., Liu, Y., Feit, E. M., Fuchs, E., Klampfl, E., Michalek, J. J., Will subsidies drive electric vehicle adoption? Measuring consumer preferences in the US and China. *Transportation Research Part A: Policy and Practice*, 73, 96-112, 2015.
- [20] Sharmila, B., Srinivasan, K., Devasena, D., Suresh, M., Panchal, H., Ashokkumar, R., Shah, R. R., Modelling and performance analysis of electric vehicle. *International Journal of Ambient Energy*, 43(1), 5034-5040, 2022.
- [21] Zeng, D., Dong, Y., Cao, H., Li, Y., Wang, J., Li, Z., Hauschild, M. Z., Are the electric vehicles more sustainable than the conventional ones? Influences of the assumptions and modeling approaches in the case of typical cars in China. *Resources, Conservation and Recycling*, 167, 105210, 2021.
- [22] Gnann, T., Funke, S., Jakobsson, N., Plötz, P., Sprei, F., & Wietschel, M. (2020). *Future of the European EV market – drivers and barriers towards success*, Fraunhofer ISI, [Online]. Available: <https://www.isi.fraunhofer.de/content/dam/isi/dokumente/sustainability-innovation/2020/Future-of-the-European-EV-Market.pdf>. [Accessed: Apr. 04, 2023].
- [23] Hall, D., Lutsey, N., *Electric vehicle charging guide for cities*, International Council on Clean Transportation, Feb. 2020, Washington DC, USA., 2020.
- [24] Dünya Enerji Konseyi (DEK), *Global electric vehicle Outlook*, [Online]. Available: <https://iea.blob.core.windows.net/assets/ad8fb04c-4f75-42fc-973a6e54c8a4449a/GlobalElectricVehicleOutlook2022.pdf> [Accessed: Oct. 21, 2022], 2022.
- [25] Türkiye Elektrikli ve Hibrid Araçlar Platformu (TEHAD). *Elektrikli araçlar*, [Online]. Available: <http://tehad.org/> [Accessed: Sept. 26, 2022], 2022.
- [26] Türkiye'nin Girişimi Otomobil Gurubu (TOGG). *Elektrikli araçlar*, [Online]. Available: <https://www.togg.com.tr/> [Accessed: Sept. 26, 2022], 2022.
- [27] İndigo, *Türkiye elektrikli araçlara hazır mı?*, [Online]. Available: <https://indigodergisi.com/2018/04/turkiye-elektrikli-araclara-hazir-mi/> [Accessed: Sept. 12, 2020], 2018.
- [28] İndigo, *Türkiye elektrikli araçlara hazır mı?*, [Online]. Available: <https://indigodergisi.com/2022/04/turkiye-elektrikli-araclara-hazir-mi/> [Accessed: Sept. 10, 2022], 2022.
- [29] İspark, *Otoparklarımız*, [Online]. Available: <https://ispark.istanbul/otoparklarimiz/> [Accessed: Oct. 10, 2021], 2018.

- [30] Driving, *Buying guide for Toyota prius*, [Online]. Available: <https://www.driving.co.uk/car-clinic/buying-guide-toyota-prius-2000-to-present/> [Accessed: Oct. 26, 2020], 2018.
- [31] Ondokuz Mayıs Üniversitesi (OMU), *OMÜ kampüs*, [Online]. Available: <https://omu.edu.tr> [Accessed: Sept. 26, 2022], 2022.